Local Position-space Two-nucleon Potentials from Leading to Fourth Order of Chiral Effective Field Theory

A Dissertation

Presented in Partial Fulfilment of the Requirements for the

Degree of Doctor of Philosophy

with a

Major in Physics

in the

College of Graduate Studies

University of Idaho

by

Sanjoy Kumar Saha

Approved By:

Major Professor: Ruprecht Machleidt, Ph.D.

Committee Members: Francesca Sammarruca, Ph.D.; Andreas Vasdekis, Ph.D.;

Hasan Jamil, Ph.D.

Department Administrator: John Hiller, Ph.D.

August 2022

Abstract

We present local, position-space chiral NN potentials through four orders of chiral EFT ranging from leading order (LO) to next-to-next-to-next-to-leading order ($\mathrm{N^3LO}$, fourth order) of the Δ-less version of the theory. The long-range parts of these potentials are fixed by the very accurate πN LECs as determined in the Roy-Steiner equations analysis. At the highest order ($\mathrm{N^3LO}$), the NN data below 190 MeV laboratory energy are reproduced with the acceptable χ^2/datum of 1.45. These NN potentials may serve as a solid basis for systematic *ab initio* calculations of nuclear structure and reactions that allow for a comprehensive error analysis. In particular, the order by order development of the potentials will make possible a reliable determination of the truncation error at each order. Our new family of local position-space potentials differs from existing potentials of this kind by a weaker tensor force as reflected in relatively low D-state probabilities of the deuteron ($P_D \lesssim 4.0$ % for our $\mathrm{N^3LO}$ potentials) and predictions for the triton binding energy above 8.00 MeV (from two-body forces alone). As a consequence, our potentials may lead to different predictions when applied to light and intermediate-mass nuclei in *ab initio* calculations and, potentially, help solving some of the outstanding problems in microscopic nuclear structure.

Acknowledgements

I cannot adequately emphasize my appreciation and gratitude towards my advisor Dr. Ruprecht Machleidt. Dr. Ruprecht's excellent guidance and tutelage has imparted to me the knowledge and skills necessary to successfully navigate the rigors of doctoral research. His patience, kindness and belief in me has enabled my achievements and success, and without which I certainly would not have been able to complete my studies. His first-rate instruction in the graduate courses of Quantum Mechanics I and II were instrumental to developing my understanding as a physicist and to building the foundation required to continuing my studies. His continuous support, encouragement, open communication and patient explanations provided the scholastic environment for developing an understanding of the intricacies contained within this work. I am deeply indebted to Dr. Rupprecht and am sincerely grateful for his excellent work as my mentor.

I would like to give a special thanks to my committee member and instructor Dr. Francesca Sammarruca. Dr. Francesca's unparalleled quality in teaching Classical Mechanics and Mathemetical Method provided an important framework for my success throughout my graduate studies. Her combined rigor, wit and lucid explanations made tedious subjects like Classical mechanics, Mathemetical Methods and Partical and nuclear physics not only understandable, but enjoyable. I am deeply indebted and without which I certainly could not have completed my studies.

I would like to thank my committee members Dr. Hasan Jamil and Dr. Andreas Vasdekis for their time and effort in working with me and on my committee during this especially difficult year. I would also like to thank Dr. Leah Bergman for her time on my committee. I would also like to give a big thank you to Jessica DeWitt for all her assistance in administrative and bureaucratic matters and working tirelessly to ensure all deadlines were met.

I would like to thank Dr. Yevgen and Dr. Entem for their support and direction of

my research work.

I would like acknowledge and thank my fellow physics cohorts : Steven Kreyche, Ross Miller, Michael Hesler. You all were good friends and the best of study companions. The hours spent doing homework, preparing for the quals, laughing, joking and crying together will not be forgotten, I couldn't have done it without you guys. A very special thanks to Steven and Dr. Zahid for all of their support.

Lastly I would like to acknowledge and thank my parents, my sister and all of my friends who provided mental support and encouragement throughout my time at the University of Idaho.

Table of Contents

List of Tables

List of Figures

CHAPTER 1

Introduction

The understanding of the nuclear force and the structure of nuclei has been a long-standing desire for nuclear physicists. In principal, the derivation of the nuclear force should be based upon quantum chromodynamics (QCD), since it is the fundamental theory of strong interactions. However, in the low energy regime typical for nuclear physics, QCD is non-perturbative, which makes it difficult to find analytic solutions. Breakthrough happened when an effective field theory (EFT) concept was introduced and applied to low energy QCD. As Weinberg proposed, one has to write down the most general Lagrangian consistent with the assumed symmetry principles, particularly the (broken) chiral symmetry of QCD [1]. At low energy, pions (the Goldstone bosons of the broken symmetry) and nucleons rather than quarks and gluons are the effective degree of freedom. Broken chiral symmetry is a crucial constraint that generates and controls the dynamics and establishes a clear connection with QCD [2].

A primary goal of theoretical nuclear physics is to explain nuclear structure and reactions in terms of the forces between nucleons—in present-day popular jargon dubbed the *ab initio* approach. The current prevailing belief in the community is that chiral effective field theory (EFT) is best suited to provide those forces, because it can be related to low-energy QCD in a straight-forward way and produces abundant three-nucleon forces (3NFs) needed for any quantitative nuclear structure prediction [2, 3, 4, 5].

Since chiral EFT is a low-momentum expansion, most chiral NN potentials of the past have been developed in momentum space–and are non-local. However, this feature makes them unsuitable for a large group of *ab initio* few- and many-body algorithms, particularly, the ones known as quantum Monte Carlo (QMC) methods [6, 7]. Variational Monte Carlo (VMC) and Green's Function Monte Carlo (GFMC) techniques provide reliable solutions of the many-body Schrődinger equation for, presently, up to 12 nucleons. Spectra, form factors, transitions, low-energy scattering, and response functions for light nuclei have been

successfully calculated using QMC methods [8]. A further extension, the Auxiliary Field Diffusion Monte Carlo (AFDMC) [6, 7], additionally samples the spin-isospin degrees of freedom, thus, making possible the study of neutron matter. In summary, QMC techniques have substatially contributed to the progress in *ab initio* nuclear structure of the past 20+ years, and will continue to do so. Thus, it is important that high-quality nuclear interactions are available for application by these promising many-body methods.

An important advantage of chiral EFT is that it allows for a systematic quantification of the uncertainties of the predictions. For this it is necessary to conduct calculations at different orders of the chiral expansion. However, so far, *local* chiral NN potentials have been developed only at next-to-next-to-leading order (NNLO) [9] or in the hybrid format, NNLO/N^{3}LO [10, 11], where two-pion exchange (2PE) contributions are included up to NNLO and contact terms up to next-to-next-to-next-to-leading order (N^{3}LO). To make proper uncertainty quantifications possible, local chiral NN potentials at all orders from leading order (LO) to N^{3}LO (and, if necessary, even beyond) are needed. It is the purpose of this work to construct such local NN potentials of high quality and make them available for QMC calculations as well as any other purposes where they can be of use. We will develope these potentials within the Δ-less theory, since—in contrast to earlier claims—it has been shown recently [12] that there is no advantage to the Δ-full theory.

This dissertation is organized as follows: In Chapter II, we present the expansion of the NN potential through all orders from LO to N^{3}LO. The reproduction of the NN scattering data and the deuteron properties are given in Chapter III. Uncertainty quantification is considered in Chapter IV. Chapter V concludes the thesis.

CHAPTER 2

The chiral NN potential

2.1 Effective Langrangians

In the Δ-less version of chiral EFT, which is the one we are applying, the relevant degrees of freedom are pions (Goldstone bosons) and nucleons. Consequently, the effective Lagrangian is subdivided into the following pieces,

$$\mathcal{L}_{\rm eff} = \mathcal{L}_{\pi\pi} + \mathcal{L}_{\pi N} + \mathcal{L}_{NN} + \dots \,, \tag{2.1}$$

where $\mathcal{L}_{\pi\pi}$ deals with the dynamics among pions, $\mathcal{L}_{\pi N}$ describes the interaction between pions and a nucleon, and $\mathcal{L}_{NN}$ contains two-nucleon contact interactions which consist of four nucleon-fields (four nucleon legs) and no meson fields. The ellipsis stands for terms that involve two nucleons plus pions and three or more nucleons with or without pions, relevant for nuclear many-body forces. Since the interactions of Goldstone bosons must vanish at zero momentum transfer and in the chiral limit ($m_\pi \to 0$), the low-energy expansion of the effective Lagrangian is arranged in powers of derivatives and pion masses, implying to following organization:

$$\begin{aligned}
\mathcal{L}_{\pi\pi} &= \mathcal{L}^{(2)}_{\pi\pi} + \mathcal{L}^{(4)}_{\pi\pi} + \dots \,, && (2.2)\\
\mathcal{L}_{\pi N} &= \mathcal{L}^{(1)}_{\pi N} + \mathcal{L}^{(2)}_{\pi N} + \mathcal{L}^{(3)}_{\pi N} + \mathcal{L}^{(4)}_{\pi N} + \dots \,, && (2.3)\\
\mathcal{L}_{NN} &= \mathcal{L}^{(0)}_{NN} + \mathcal{L}^{(2)}_{NN} + \mathcal{L}^{(4)}_{NN} + \dots \,, && (2.4)
\end{aligned}$$

where the superscript refers to the number of derivatives or pion mass insertions (chiral dimension) and the ellipses stand for terms of higher dimensions. We use the heavy-baryon formulation of the Lagrangians, the explicit expressions of which can be found in Ref. [2].

2.2 Power counting

Based upon the above Langrangians, an infinite number of diagrams contributing to the interactions among nucleons can be drawn. Nuclear potentials are defined by the irreducible types of these graphs. By definition, an irreducible graph is a diagram that cannot be separated into two by cutting only nucleon lines. These graphs are then analyzed in terms of powers of small external momenta over the breakdown scale: $(p/\Lambda_b)^\nu$, where p is generic for a momentum (nucleon three-momentum or pion four-momentum) or a pion mass and $\Lambda_b \sim m_\rho \sim 0.7$ GeV is the breakdown scale [13]. Determining the power ν has become know as power counting.

Following the Feynman rules of covariant perturbation theory, a nucleon propagator is p^{-1}, a pion propagator p^{-2}, each derivative in any interaction is p, and each four-momentum integration p^4. This is also known as naive dimensional analysis or Weinberg counting.

Since we use the heavy-baryon formalism, we encounter terms which include factors of p/M_N, where M_N denotes the nucleon mass. We count the order of such terms by the rule $p/M_N \sim (p/\Lambda_b)^2$, for reasons explained in Ref. [1].

Applying some topological identities, one obtains for the power of a connected irreducible diagram involving A nucleons [1, 2]

$$\nu = -2 + 2A - 2C + 2L + \sum_i \Delta_i \,, \tag{2.5}$$

with

$$\Delta_i \equiv d_i + \frac{n_i}{2} - 2 \,, \tag{2.6}$$

where L denotes the number of loops in the diagram; d_i is the number of derivatives or pion-mass insertions and n_i the number of nucleon fields (nucleon legs) involved in vertex i; the sum runs over all vertexes i contained in the connected diagram under consideration. Note that $\Delta_i \geq 0$ for all interactions allowed by chiral symmetry.

An important observation from power counting is that the powers are bounded from below and, specifically, $\nu \geq 0$. This fact is crucial for the convergence of the low-momentum expansion.

For an irreducible NN diagram ($A = 2$, $C = 1$), the power formula collapses to the very simple expression

$$\nu = 2L + \sum_i \Delta_i \,, \tag{2.7}$$

which is most relevant for our current work.

In summary, the chief point of the chiral perturbation theory (ChPT) expansion of the potential is that, at a given order ν, there exists only a finite number of graphs. This is what makes the theory calculable. The expression $(p/\Lambda_\chi)^{\nu+1}$ provides an estimate of the relative size of the contributions left out and, thus, of the relative uncertainty at order ν. The ability to calculate observables (in principle) to any degree of accuracy gives the theory its predictive power.

ChPT and power counting imply that nuclear forces evolve as a hierarchy controlled by the power ν, see Fig. 2.1 for an overview. In what follows, we will focus on the two-nucleon force (2NF).

2.3 The long-range NN potential

The long-range part of the NN potential is built up from pion exchanges, which are ruled by chiral symmetry. The various pion-exchange contributions are best analyzed by the number of pions being exchanged between the two nucleons:

$$V_\pi = V_{1\pi} + V_{2\pi} + V_{3\pi} + \dots \,, \tag{2.8}$$

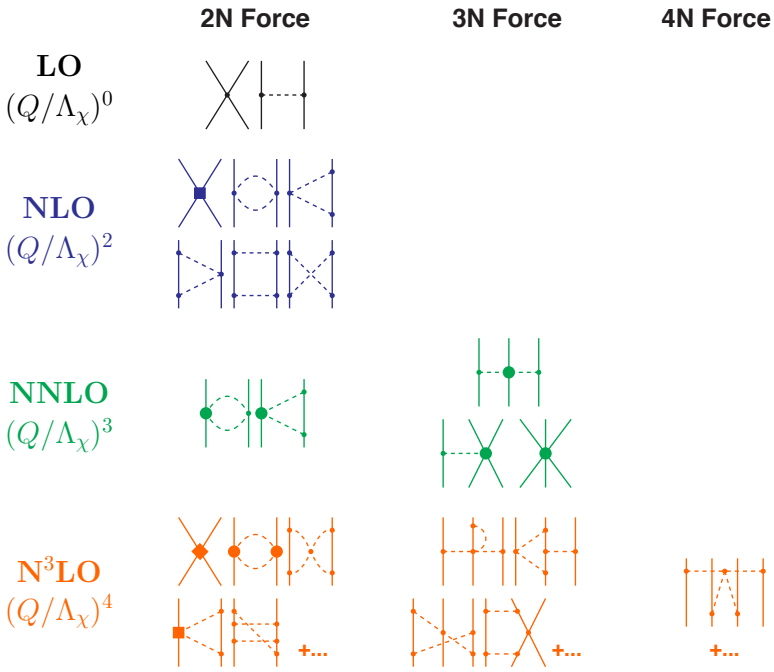

Figure 2.1: Hierarchy of nuclear forces in ChPT. Solid lines represent nucleons and dashed lines pions. Small dots, large solid dots, solid squares, and solid diamonds denote vertexes of index $\Delta_i = 0$, 1, 2, and 4, respectively. Further explanations are given in the text.

where the meaning of the subscripts is obvious and the ellipsis represents 4π and higher pion exchanges. For each of the above terms, we have a low-momentum expansion:

$$V_{1\pi} = V_{1\pi}^{(0)} + V_{1\pi}^{(2)} + V_{1\pi}^{(3)} + V_{1\pi}^{(4)} + \dots , \tag{2.9}$$

$$V_{2\pi} = V_{2\pi}^{(2)} + V_{2\pi}^{(3)} + V_{2\pi}^{(4)} + \dots , \tag{2.10}$$

$$V_{3\pi} = V_{3\pi}^{(4)} + \dots , \tag{2.11}$$

where the superscript denotes the order ν of the expansion. Higher order corrections to the one-pion exchange (1PE) are taken care of by mass and coupling constant renormalizations. Note also that, on shell, there are no relativistic corrections. Thus, $V_{1\pi} = V_{1\pi}^{(0)}$ through all orders. The leading 3π-exchange contribution that occurs at N^{3}LO, $V_{3\pi}^{(4)}$, has been calculated in Refs. [14, 15] and found to be negligible. We, therefore, omit it.

Table 2.1: The πN LECs as determined in the Roy-Steiner-equation analysis of πN scattering conducted in Ref. [21]. The given orders of the chiral expansion refer to the NN system. The c_i and $\bar{d}_i$ are the LECs of the second and third order πN Lagrangian [2] and are in units of GeV^{-1} and GeV^{-2}, respectively. The uncertainties in the last digits are given in parentheses after the values. We use the central values.

	NNLO	N^{3}LO
c_1	–0.74(2)	–1.07(2)
c_2		3.20(3)
c_3	–3.61(5)	–5.32(5)
c_4	2.44(3)	3.56(3)
$\bar{d}_1 + \bar{d}_2$		1.04(6)
$\bar{d}_3$		–0.48(2)
$\bar{d}_5$		0.14(5)
$\bar{d}_{14} - \bar{d}_{15}$		–1.90(6)

Order by order, the long-range NN potential then builds up as follows:

$$V_\pi^{\mathrm{LO}} = V_{1\pi}^{(0)}\,, \tag{2.12}$$

$$V_\pi^{\mathrm{NLO}} = V_\pi^{\mathrm{LO}} + V_{2\pi}^{(2)}\,, \tag{2.13}$$

$$V_\pi^{\mathrm{NNLO}} = V_\pi^{\mathrm{NLO}} + V_{2\pi}^{(3)}\,, \tag{2.14}$$

$$V_\pi^{\mathrm{N3LO}} = V_\pi^{\mathrm{NNLO}} + V_{2\pi}^{(4)}\,. \tag{2.15}$$

We note that we add to V_π^{N3LO} the $1/M_N$ corrections of the NNLO 2PE proportional to c_i (cf. Table 2.1). This correction is proportional to c_i/M_N (cf. Fig. A.3 and Appendix A.5, below) and appears nominally at fifth order, but we include it at fourth order. As demonstrated in Ref. [16], the 2PE football diagram proportional to c_i^2 that appears at N^{3}LO (Fig. A.2(a) and Appendix A.4.1) is unrealistically attractive, while the c_i/M_N correction is large and repulsive. Therefore, it makes sense to group these diagrams together to arrive at a more realistic intermediate-range attraction at N^{3}LO. This is common practice and has been done so in Refs. [17, 19, 20].

The explicit mathematical expressions for the pion-exchanges up to N^{3}LO are very involved. We have, therefore, moved them into the Appendix A.

Table 2.2: Basic constants used throughout this work [22].

puantity	Value
Axial-vector coupling constant g_A	1.29
Pion-decay constant f_π	92.4 MeV
Charged-pion mass $m_{\pi^\pm}$	139.5702 MeV
Neutral-pion mass m_{π^0}	134.9766 MeV
Average pion-mass $\bar{m}_\pi$	138.0390 MeV
Proton mass M_p	938.2720 MeV
Neutron mass M_n	939.5654 MeV
Average nucleon-mass $\bar{M}_N$	938.9183 MeV

Chiral symmetry establishes a link between the dynamics in the πN-system and the NN-system through common low-energy constants (LECs). Therefore, consistency requires that we use the LECs for subleading πN-couplings as determined in the analysis of low-energy πN-scattering. Currently, the most reliable πN analysis is the one by Hoferichter and Ruiz de Elvira *et al.* [21], in which the Roy-Steiner equations are applied. These LECs carry very small uncertainties (cf. Table 2.1); in fact, the uncertainties are so small that they are negligible for our purposes. This makes the variation of the πN LECs in NN potential construction obsolete and reduces the error budget in applications of these potentials. For the potentials constructed in this thesis, the central values of Table 2.1 are applied. Other constants involved in our potential construction are shown in Table 2.2.

2.4 The short-range NN potential

The short-range NN potential is described by contributions of the contact type, which are constrained by parity, time-reversal, and the usual invariances, but not by chiral symmetry. Because of parity and time-reversal only even powers of momentum are allowed. Thus, the expansion of the contact potential is formally written as

$$V_{\rm ct} = V_{\rm ct}^{(0)} + V_{\rm ct}^{(2)} + V_{\rm ct}^{(4)} + + \dots \ , \tag{2.16}$$

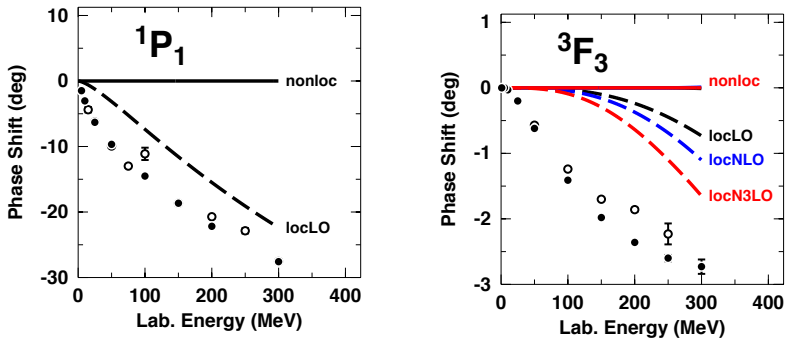

Figure 2.2: Left panel: $^1P_1$ phase shifts for an order zero (i.e., LO) contact term with nonlocal regulator (solid black line, "nonloc") versus the same term multiplied with a local regulator (dashed black line, "locLO"). Right panel: $^3F_3$ phase shifts for contact terms at order LO, NLO, and N^{3}LO with nonlocal regulator (solid red line, "nonloc") versus the same orders multiplied with a local regulator (dashed lines at orders as denoted). The filled and open circles represent the results from the Nijmegen multi-energy np phase-shift analysis [30] and the GWU single-energy np analysis SP07 [34], respectively.

where the superscript denotes the power or order.

In principle, the most general set of contact terms at each order is provided by all combinations of spin, isospin, and momentum operators that are allowed by the usual symmetries [23] at the given order. Two momenta are available, namely, the final and initial nucleon momenta in the center-of-mass system, $\vec{p}\,'$ and $\vec{p}$. This can be reformulated in terms of two alternative momenta, viz., the momentum transfer $\vec{q} = \vec{p}\,' - \vec{p}$ and the average momentum $\vec{k} = (\vec{p}\,' + \vec{p})/2$. Functions of $\vec{q}$ lead to local interactions, that is, to functions of the relative distance $\vec{r}$ between the two nucleons after Fourier transform. On the other hand, functions of $\vec{k}$ lead to nonlocal interactions.

Since ChPT is a low-momentum expansion, it requires cutting off high momenta to avoid divergencies. This is achieved by mutiplying the potential with a regulator function that suppresses the large momenta (or, equivalently, the short distances). Depending on the type of momenta used, the regulator can be local or nonlocal.

When chiral NN potentials are constructed in momentum-space and regulated by nonlocal cutoff functions [2], then it is possible to reduce the number of contact operators (by a factor of two) due to Fierz ambiguity [24, 25] which is a consequence of the fact that nucleons

are Fermions and obey the Pauli exclusion principle. However, for the reasons stated in the Introduction, we wish to construct NN potentials which are strictly local, implying that we have to use local regulators.

When a local (regulator) function is applied to the contact terms, then the Fierz ambiguity is violated. To provide a simple example of this, consider a contact operator of order zero ($\sim Q^0$, LO). After a partial-wave expansion, such operator produces no contributions for states with orbital amgular momentum $L > 0$, i.e., P and higher partial waves. However, this property is violated when the operator is multiplied with a local regulator function. We demonstrate this fact in Fig. 2.2, where, in the left panel, we show phase shifts in the $^1P_1$ state: The solid line ("nonloc") shows the phase shifts when the LO contact term is multiplied with a nonlocal cutoff function, which does not violate Fierz reordering and, therefore is zero for all energies. However, when multiplied by a local regulator, the dashed curve ("locLO") is obtained, which is almost as large as the empirical phase shifts. Thus, the violation is almost 100% as compared to experiment.

This violation by nonlocal regulators continues through higher orders. As an example, we show in the right panel of Fig. 2.2 the phase shifts in an F-wave, where polynomial terms up to fourth order do not contribute which, as demonstrated in the figure, is, indeed, true for nonlocal cutoffs (solid red curve, "nonloc"). However, when local functions are applied, then at orders Q^0, Q^2, and Q^4, respectively, the contributions are not zero as demonstrated by the dashed curves denoted by "locLO", "locNLO", "locN3LO", respectively. In this F-wave, the final violation amounts to about 50% of experiment.

Thus, when applying local regulators, terms beyond the given order are affected, which is the reason for the violation of Fierz rearrangement. As demonstrated in Fig. 2.2 by the dashed lines, these violations are large. Since it does not make sense to apply a symmetry that is invalid for the problem under consideration, we will not apply Fierz reordering to the contact terms and, hence, use for the contacts all combinations of spin, isospin, and momentum operators that are allowed by the usual symmetries. To enforce locality, we

will use only the momentum operator $\vec{q}$ (except in the momentum-representation of the angular-momentum operator, $[-i(\vec{q}\times\vec{k})\,]$).

We note that this is also the philosopy of the Argonne v_{18} potential (AV18) [26], which includes 14 charge-independent operators. Not accidentally, we will also have 14 contact operators at N^{3}LO (see below) which are all equivalent to the 14 operators of the AV18 potential. Our contacts at LO and NLO are just the lower order contributions to those 14 operators (most of which vanish).

We will now present the explicit expressions for the contact operators, order by order.

2.4.1 Leading order

In momentum-space, the LO or zeroth order contact terms are given by

$$V_{\rm ct}^{(0)}(q) \;=\; (C_c + C_\tau\,\boldsymbol{\tau}_1\cdot\boldsymbol{\tau}_2 + C_\sigma\,\vec{\sigma}_1\cdot\vec{\sigma}_2 + C_{\sigma\tau}\,\vec{\sigma}_1\cdot\vec{\sigma}_2\;\boldsymbol{\tau}_1\cdot\boldsymbol{\tau}_2)\,f_{\rm ct}(q) \qquad (2.17)$$

with regulator function

$$f_{\rm ct}(q) = e^{-(q/\Lambda)^2} \qquad (2.18)$$

and Λ a momentum cutoff. The operators $\vec{\sigma}_{1,2}$ and $\boldsymbol{\tau}_{1,2}$ denote the spin and isospin of nucleon 1 and 2, respectively.

In position space, $V_{\rm ct}^{(0)}(q)$ translates into

$$\widetilde{V}_{\rm ct}^{(0)}(r) \;=\; (C_c + C_\tau\,\boldsymbol{\tau}_1\cdot\boldsymbol{\tau}_2 + C_\sigma\,\vec{\sigma}_1\cdot\vec{\sigma}_2 + C_{\sigma\tau}\,\vec{\sigma}_1\cdot\vec{\sigma}_2\;\boldsymbol{\tau}_1\cdot\boldsymbol{\tau}_2)\;{}^{\rm ct}\widetilde{V}_C^{(0)}(r) \qquad (2.19)$$

with

$${}^{\rm ct}\widetilde{V}_C^{(0)}(r) = \widetilde{f}_{\rm ct}(r) = \frac{1}{\pi^{3/2}\,R_{\rm ct}^3}\,e^{-(r/R_{\rm ct})^2}\,, \qquad (2.20)$$

the Fourier transform of $f_{\rm ct}(q)$ and $R_{\rm ct} = 2/\Lambda$. Note that we use units such that $\hbar = c = 1$.

2.4.2 Next-to-leading order

In momentum-space, the NLO or second order contact contribution is

$$\begin{aligned} V_{\rm ct}^{(2)}(\vec{p}\,',\vec{p}) &= \Big\{ (C_1 + C_2\,\boldsymbol{\tau}_1\cdot\boldsymbol{\tau}_2 + C_3\,\vec{\sigma}_1\cdot\vec{\sigma}_2 + C_4\,\vec{\sigma}_1\cdot\vec{\sigma}_2\;\boldsymbol{\tau}_1\cdot\boldsymbol{\tau}_2)\; q^2 \\ &\quad + (C_5 + C_6\,\boldsymbol{\tau}_1\cdot\boldsymbol{\tau}_2)\;\widehat{S}_{12}(\vec{q}) \\ &\quad + (C_7 + C_8\,\boldsymbol{\tau}_1\cdot\boldsymbol{\tau}_2)\;\Big[-i\vec{S}\cdot(\vec{q}\times\vec{k})\Big]\Big\}\, f_{\rm ct}(q)\,, \end{aligned} \tag{2.21}$$

where $\vec{S} = (\vec{\sigma}_1 + \vec{\sigma}_2)/2$ denotes the total spin and

$$\widehat{S}_{12}(\vec{q}) = 3\,\vec{\sigma}_1\cdot\vec{q}\;\;\vec{\sigma}_2\cdot\vec{q} - q^2\,\vec{\sigma}_1\cdot\vec{\sigma}_2 \tag{2.22}$$

is the tensor operator in momentum-space.

Fourier transform of the above creates the second order contact contribution in position space

$$\begin{aligned} \widetilde{V}_{\rm ct}^{(2)}(\vec{r}) &= (C_1 + C_2\,\boldsymbol{\tau}_1\cdot\boldsymbol{\tau}_2 + C_3\,\vec{\sigma}_1\cdot\vec{\sigma}_2 + C_4\,\vec{\sigma}_1\cdot\vec{\sigma}_2\;\boldsymbol{\tau}_1\cdot\boldsymbol{\tau}_2)\;\;{}^{\rm ct}\widetilde{V}_C^{(2)}(r) \\ &\quad + (C_5 + C_6\,\boldsymbol{\tau}_1\cdot\boldsymbol{\tau}_2)\;S_{12}(\hat{r})\;\;{}^{\rm ct}\widetilde{V}_T^{(2)}(r) \\ &\quad + (C_7 + C_8\,\boldsymbol{\tau}_1\cdot\boldsymbol{\tau}_2)\;(\vec{L}\cdot\vec{S})\;\;{}^{\rm ct}\widetilde{V}_{LS}^{(2)}(r)\,, \end{aligned} \tag{2.23}$$

where

$$S_{12}(\hat{r}) = 3\vec{\sigma}_1\cdot\hat{r}\;\;\vec{\sigma}_2\cdot\hat{r} - \vec{\sigma}_1\cdot\vec{\sigma}_2 \tag{2.24}$$

denotes the standard position-space tensor operator with $\hat{r} = \vec{r}/r$, and $\vec{L}$ is the operator of

total angular momentum. Furthermore,

$$
\begin{aligned}
{}^{\rm ct}\widetilde{V}_C^{(2)}(r) &= -\widetilde{f}_{\rm ct}^{(2)}(r) - \frac{2}{r}\,\widetilde{f}_{\rm ct}^{(1)}(r)\,, && (2.25)\\
{}^{\rm ct}\widetilde{V}_T^{(2)}(r) &= -\widetilde{f}_{\rm ct}^{(2)}(r) + \frac{1}{r}\,\widetilde{f}_{\rm ct}^{(1)}(r)\,, && (2.26)\\
{}^{\rm ct}\widetilde{V}_{LS}^{(2)}(r) &= -\frac{1}{r}\,\widetilde{f}_{\rm ct}^{(1)}(r)\,, && (2.27)
\end{aligned}
$$

with

$$
\widetilde{f}_{\rm ct}^{(n)}(r) = \frac{d^n\,\widetilde{f}_{\rm ct}(r)}{dr^n}\,. \qquad (2.28)
$$

2.4.3 Next-to-next-to-next-to-leading order

In momentum-space, the N^{3}LO or fourth order contact contribution is assumed to be

$$
\begin{aligned}
V_{\rm ct}^{(4)}(\vec{p}\,',\vec{p}) &= \Big\{ (D_1 + D_2\,\boldsymbol{\tau}_1\cdot\boldsymbol{\tau}_2 + D_3\,\vec{\sigma}_1\cdot\vec{\sigma}_2 + D_4\,\vec{\sigma}_1\cdot\vec{\sigma}_2\;\boldsymbol{\tau}_1\cdot\boldsymbol{\tau}_2)\;q^4 \\
&\quad + (D_5 + D_6\,\boldsymbol{\tau}_1\cdot\boldsymbol{\tau}_2)\;q^2\,\widehat{S}_{12}(\vec{q}) \\
&\quad + (D_7 + D_8\,\boldsymbol{\tau}_1\cdot\boldsymbol{\tau}_2)\;q^2\,\Big[-i\vec{S}\cdot(\vec{q}\times\vec{k})\Big] \\
&\quad + (D_9 + D_{10}\,\boldsymbol{\tau}_1\cdot\boldsymbol{\tau}_2)\,\Big[-i\vec{S}\cdot(\vec{q}\times\vec{k})\Big]^2 \\
&\quad + (D_{11} + D_{12}\,\boldsymbol{\tau}_1\cdot\boldsymbol{\tau}_2 + D_{13}\,\vec{\sigma}_1\cdot\vec{\sigma}_2 + D_{14}\,\vec{\sigma}_1\cdot\vec{\sigma}_2\;\boldsymbol{\tau}_1\cdot\boldsymbol{\tau}_2) \\
&\quad \times\Big[-i(\vec{q}\times\vec{k})\Big]^2\Big\} f_{\rm ct}(q) \qquad (2.29)
\end{aligned}
$$

In position-space, the N^{3}LO or fourth order contact contribution then is

$$\begin{aligned}
\widetilde{V}_{\rm ct}^{(4)}(\vec{r}) &= (D_1 + D_2\,\boldsymbol{\tau}_1\cdot\boldsymbol{\tau}_2 + D_3\,\vec{\sigma}_1\cdot\vec{\sigma}_2 + D_4\,\vec{\sigma}_1\cdot\vec{\sigma}_2\;\boldsymbol{\tau}_1\cdot\boldsymbol{\tau}_2)\;{}^{\rm ct}\widetilde{V}_C^{(4)}(r) \\
&\quad + (D_5 + D_6\,\boldsymbol{\tau}_1\cdot\boldsymbol{\tau}_2)\;S_{12}(\hat{r})\;{}^{\rm ct}\widetilde{V}_T^{(4)}(r) \\
&\quad + (D_7 + D_8\,\boldsymbol{\tau}_1\cdot\boldsymbol{\tau}_2)\;(\vec{L}\cdot\vec{S})\;{}^{\rm ct}\widetilde{V}_{LS}^{(4)}(r) \\
&\quad + (D_9 + D_{10}\,\boldsymbol{\tau}_1\cdot\boldsymbol{\tau}_2)\;(\vec{L}\cdot\vec{S})^2\;{}^{\rm ct}\widetilde{V}_{LS2}^{(4)}(r) \\
&\quad + (D_{11} + D_{12}\,\boldsymbol{\tau}_1\cdot\boldsymbol{\tau}_2 + D_{13}\,\vec{\sigma}_1\cdot\vec{\sigma}_2 + D_{14}\,\vec{\sigma}_1\cdot\vec{\sigma}_2\;\boldsymbol{\tau}_1\cdot\boldsymbol{\tau}_2) \\
&\quad \times\vec{L}^2\,{}^{\rm ct}\widetilde{V}_{LL}^{(4)}(r)\,, \qquad (2.30)
\end{aligned}$$

with

$$\begin{aligned}
{}^{\rm ct}\widetilde{V}_C^{(4)}(r) &= \widetilde{f}_{\rm ct}^{(4)}(r) + \frac{4}{r}\,\widetilde{f}_{\rm ct}^{(3)}(r)\,, &(2.31)\\
{}^{\rm ct}\widetilde{V}_T^{(4)}(r) &= \widetilde{f}_{\rm ct}^{(4)}(r) + \frac{1}{r}\,\widetilde{f}_{\rm ct}^{(3)}(r) - \frac{6}{r^2}\,\widetilde{f}_{\rm ct}^{(2)}(r) + \frac{6}{r^3}\,\widetilde{f}_{\rm ct}^{(1)}(r)\,, &(2.32)\\
{}^{\rm ct}\widetilde{V}_{LS}^{(4)}(r) &= \frac{1}{r}\,\widetilde{f}_{\rm ct}^{(3)}(r) + \frac{2}{r^2}\,\widetilde{f}_{\rm ct}^{(2)}(r) - \frac{2}{r^3}\,\widetilde{f}_{\rm ct}^{(1)}(r)\,, &(2.33)\\
{}^{\rm ct}\widetilde{V}_{LS2}^{(4)}(r) &= \frac{1}{r^2}\,\widetilde{f}_{\rm ct}^{(2)}(r) - \frac{1}{r^3}\,\widetilde{f}_{\rm ct}^{(1)}(r)\,, &(2.34)\\
{}^{\rm ct}\widetilde{V}_{LL}^{(4)}(r) &= \frac{1}{r^2}\,\widetilde{f}_{\rm ct}^{(2)}(r) - \frac{1}{r^3}\,\widetilde{f}_{\rm ct}^{(1)}(r)\,, &(2.35)
\end{aligned}$$

where from the Fourier transforms of Eqs. (2.29) and (2.29) we retained only the local terms [10].

2.5 Charge dependence

This is to summarize what charge-dependence we include. Through all orders, we take the charge-dependence of the 1PE due to pion-mass splitting into account, Eqs. (A.10) - (A.13). Charge-dependence is seen most prominently in the $^1S_0$ state at low energies, particularly, in the $^1S_0$ scattering lengths. Charge-dependent 1PE cannot explain it all. The remainder is accounted for by treating the LO contact parameters in a charge-dependent way (see

Table B.1, below). In all 2PE contributions, we apply the average pion mass, $\bar{m}_\pi$. For pp scattering at any order, we include the relativistic Coulomb potential [27, 28]. We omit irreducible π-γ exchange [29], which would affect the N^{3}LO np potential. We take nucleon-mass splitting into account by using M_p in pp scattering, M_n in nn scattering, and $\bar{M}_N$ in np scattering (see Table 2.2 for their precise values).

For a comprehensive discussion of all possible sources of charge-dependence of the NN interaction, see Ref. [2].

2.6 The full potential

The full NN potential is the sum of the long- and the short-range potentials. Order by order, this results into:

$$\widetilde{V}^{\rm LO} = \widetilde{V}^{(0)}_{1\pi} + \widetilde{V}^{(0)}_{\rm ct}\,, \tag{2.36}$$

$$\widetilde{V}^{\rm NLO} = \widetilde{V}^{\rm LO} + \widetilde{V}^{(2)}_{2\pi} + \widetilde{V}^{(2)}_{\rm ct}\,, \tag{2.37}$$

$$\widetilde{V}^{\rm NNLO} = \widetilde{V}^{\rm NLO} + \widetilde{V}^{(3)}_{2\pi}\,, \tag{2.38}$$

$$\widetilde{V}^{\rm N3LO} = \widetilde{V}^{\rm NNLO} + \widetilde{V}^{(4)}_{2\pi} + \widetilde{V}^{(4)}_{\rm ct}\,, \tag{2.39}$$

where we note again that we add to $\widetilde{V}^{(4)}_{2\pi}$ the $1/M_N$ corrections of $\widetilde{V}^{(3)}_{2\pi}$. This correction is proportional to c_i/M_N and appears nominally at fifth order, but we include it at fourth order for the reasons discussed. The explicit mathematical expressions for $\widetilde{V}^{(0)}_{1\pi}$ are given in Appendix A.1, for $\widetilde{V}^{(2)}_{2\pi}$ in Appendix A.2, for $\widetilde{V}^{(3)}_{2\pi}$ in Appendix A.3, and for $\widetilde{V}^{(4)}_{2\pi}$ in Appendices A.4 and A.5.

2.7 Regularization

All pion-exchange potentials, $\widetilde{V}_\pi(r)$, are singular at the origin and, thus, need regularization. For this purpose, we multiply the $\widetilde{V}_{1\pi}^{(0)}(r)$ potential with the regulator function

$$\widetilde{f}_{1\pi}(r) = 1 - \exp\left[-\left(\frac{r}{R_\pi}\right)^{2n}\right] \tag{2.40}$$

and all $\widetilde{V}_{2\pi}^{(\nu)}(r)$ $(\nu = 2, 3, 4)$ with

$$\widetilde{f}_{2\pi}(r) = \left[1 - \exp\left(-\frac{r^2}{R_\pi^2}\right)\right]^n \tag{2.41}$$

using $n = 5$. Note that $n = 4$ is the minimum required for $\widetilde{V}_{2\pi}^{(4)}$. As stated in Sec. 2.4, the regulator of the contacts is

$$\widetilde{f}_{\rm ct}(r) = \frac{1}{\pi^{3/2}\, R_{\rm ct}^3}\, e^{-(r/R_{\rm ct})^2}\,. \tag{2.42}$$

CHAPTER 3

NN scattering and the deuteron

Based upon the formalism presented in the previous section, we have constructed NN potentials at four different orders, namely, LO, NLO, NNLO, and N^{3}LO, cf. Sec. 2.6. At each order, we apply three different cutoff combinations $(R_\pi, R_{\rm ct})$, see Sec. 2.7 for their definitions. Specifically, we use the combinations (1.0, 0.70) fm, (1.1, 0.72) fm, and (1.2, 0.75) fm. Since we take charge dependence into account, each NN potential comes in three versions: pp, np, and nn. In this section, we will present the predictions from these potentials for NN scattering and the deuteron.

3.1 NN scattering

The free (fit) parameters of our theory are the coefficients of the contact terms presented in Sec. 2.4. The other set of parameters involved in NN potential construction are the πN LECs. We apply the ones from the very accurate Roy-Steiner analysis of Ref. [21] given in Table 2.1. We use the central values and, thus, the πN LECs are precisely fixed from the outset and no fit parameters.

Fitting proceeds in two steps. First we fit phase shifts, where the adjustment is done to the Nijmegen multi-energy analysis [30], which we perceive as the most reliable one. In the second step, the potential predictions are confronted with the experimental NN data—calculating the χ^2 as follows.

The experimental data are broken up into groups (sets) of data, A, with N_A data points and an experimental over-all normalization uncertainty Δn_A^{exp}. For datum i, x_i^{exp} is the experimental value, Δx_i^{exp} the experimental uncertainty, and x_i^{mod} the model prediction. When fitting the data of group A by a model (or a phase shift solution), the over-all normalization, n_A^{mod}, is floated and finally chosen such as to minimize the χ^2 for this group. The χ^2 is then

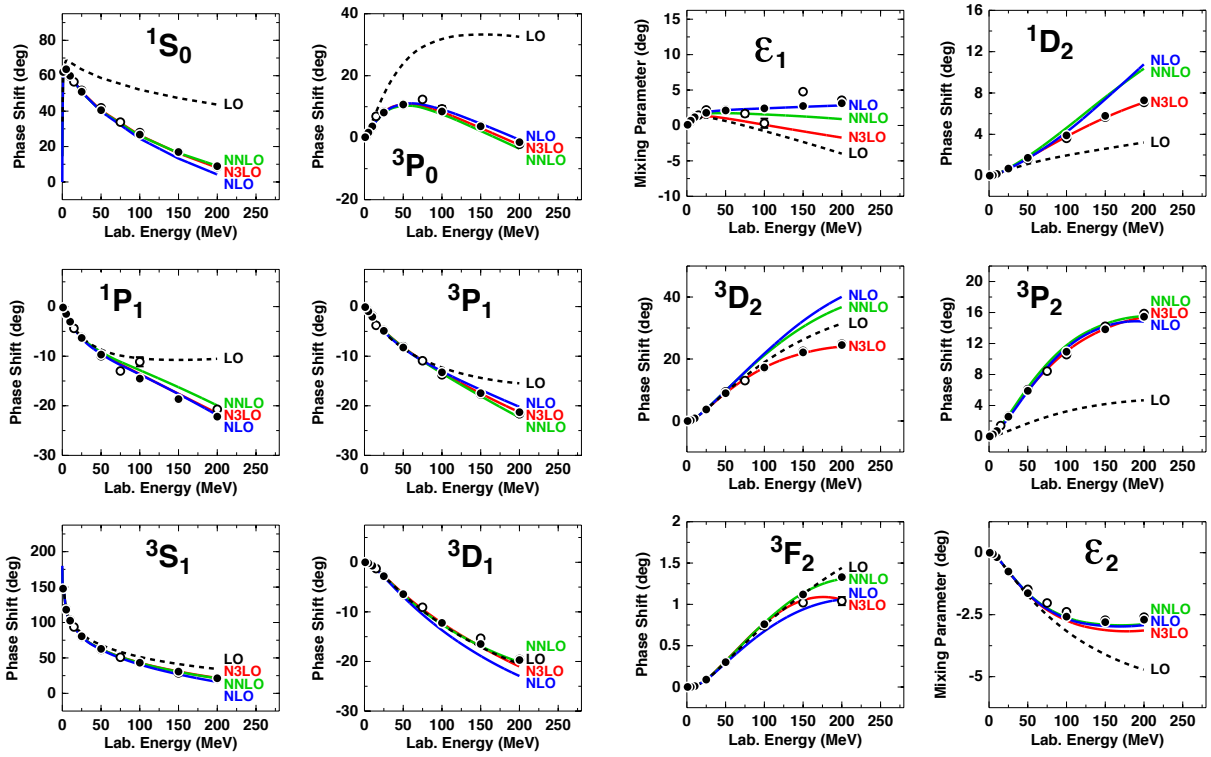

Figure 3.1: (Color online). Chiral expansion of neutron-proton scattering as represented by the phase parameters for $J \leq 2$. Four orders ranging from LO to N^{3}LO are shown as denoted. The cutoff combination $(R_\pi, R_{\rm ct}) = (1.0, 0.70)$ fm is applied in all cases. The filled and open circles represent the results from the Nijmegen multi-energy np phase-shift analysis [30] and the GWU single-energy np analysis SP07 [34], respectively.

calculated from [28]

$$\chi^2 = \sum_A \left\{ \sum_{i=1}^{N_A} \left[\frac{n_A^{mod} x_i^{mod} - x_i^{exp}}{\Delta x_i^{exp}} \right]^2 + \left[\frac{n_A^{mod} - 1}{\Delta n_A^{exp}} \right]^2 \right\} ; \tag{3.1}$$

that is, the over-all normalization of a group is treated as an additional datum. For groups of data without normalization uncertainty ($\Delta n_A^{exp} = 0$), $n_A^{mod} = 1$ is used and the second term on the r.h.s. of Eq. (3.1) is dropped. The total number of data is

$$N_{dat} = N_{obs} + N_{ne} \tag{3.2}$$

where N_{obs} denotes the total number of measured data points (observables), i. e., $N_{obs} =$

Table 3.1: χ^2/datum for the fit of the 2016 NN database [20] by NN potentials at various orders of chiral EFT applying the cutoff combination $(R_\pi, R_{\rm ct}) = (1.0, 0.70)$ fm.

$T_{\rm lab}$ bin (MeV)	No. of data	LO	NLO	NNLO	N^{3}LO
		proton-proton			
0–100	795	433	1.85	2.64	1.32
0–190	1206	363	4.60	7.84	1.33
		neutron-proton			
0–100	1180	211	1.58	2.34	1.59
0–190	1697	157	15.03	10.19	1.53
		pp plus ***np***			
0–100	1975	300	1.68	2.45	1.48
0–190	2903	243	10.74	9.23	1.45

$\sum_A N_A$; and N_{ne} is the number of experimental normalization uncertainties. We state results in terms of $\chi^2/N_{dat} \equiv \chi^2$/datum, where we use for the experimental NN data the "2016 database" defined in Ref. [20].

Each of the two steps described above, is done in two parts. In part one, we adjust the pp potential, which fixes the $T = 1$ partial waves (where T denotes the total isospin of the two-nucleon system). In part two, the charge-dependence described in Sec. 2.5 is applied to obtain the np $T = 1$ phase shifts from the pp ones. The np $T = 0$ partial-waves are then pinned down by first fitting phase shifts and, after that, minimizing the χ^2 in regard to the np data. During this last step, we allowed for minor changes of the $T = 1$ parameters (which also modifies the pp potential) to obtain an even lower overall χ^2. For more details on the NN database and the fitting procedure, see Ref. [20].

The nn potential is obtained by starting from the pp version, replacing the proton mass by the neutron mass, leaving out Coulomb, and adjusting the zeroth-order contacts such as to reproduce the empirical nn $^1S_0$ scattering length of –18.95 fm [31, 32].

The contact LECs that result from our best fits at N^{3}LO are tabulated in Appendix B.

The χ^2/datum for the reproduction of the NN data at various orders of chiral EFT are shown in Table 3.1 for different energy intervals below 190 MeV laboratory energy ($T_{\rm lab}$). The bottom line of Table 3.1 summarizes the essential results in short form. For the close

Table 3.2: Scattering lengths (a) and effective ranges (r) in units of fm as predicted by NN potentials at various orders of chiral EFT applying the cutoff combination $(R_\pi, R_{\rm ct}) = (1.0, 0.70)$ fm. (a_{pp}^C and r_{pp}^C refer to the pp parameters in the presence of the Coulomb force. a^N and r^N denote parameters determined from the nuclear force only and with all electromagnetic effects omitted.) a_{nn}^N, and a_{np} are fitted, all other quantities are predictions.

	LO	NLO	NNLO	N^{3}LO	Empirical
			$^1\boldsymbol{S_0}$		
a_{pp}^C	–7.8161	–7.8134	–7.8147	–7.8135	–7.8196(26) [28] –7.8149(29) [37]
r_{pp}^C	2.009	2.715	2.764	2.748	2.790(14) [28] 2.769(14) [37]
a_{pp}^N	—	–17.364	–17.466	–17.391	—
r_{pp}^N	—	2.788	2.834	2.818	—
a_{nn}^N	–18.950	–18.950	–18.950	–18.950	–18.95(40) [31, 32]
r_{nn}^N	1.985	2.761	2.807	2.790	2.75(11) [38]
a_{np}	–23.738	–23.738	–23.738	–23.738	–23.740(20) [36]
r_{np}	1.888	2.653	2.695	2.679	[2.77(5)] [36]
			$^3\boldsymbol{S_1}$		
a_t	5.299	5.414	5.413	5.420	5.419(7) [36]
r_t	1.586	1.750	1.747	1.756	1.753(8) [36]

to 3000 pp plus np data below 190 MeV, the χ^2/datum is 10.7 at NLO and 9.2 at NNLO. Note that the number of NN contact terms is the same for both orders. When moving on to N^{3}LO, 14 more contacts are added [Eq. (2.30)] that affect, in particular, the the $^1D_2$ and $^3D_2$ waves, which typically come out far too attractive at NLO and NNLO (Fig. 3.1). This improves the χ^2/datum to 1.45 at N^{3}LO, a respectable value.

All np phase shifts up to $J = 2$ and $T_{\rm lab} = 200$ MeV are displayed in Fig. 3.1, which reflect what just has been discussed in the context of the the χ^2.

For order N^{3}LO and cutoff combination $(R_\pi, R_{\rm ct}) = (1.0, 0.70)$ fm, we provide the numerical values for the phase shifts in Appendix C. Our pp phase shifts are the phase shifts of the nuclear plus relativistic Coulomb interaction with respect to Coulomb wave functions. Note, however, that for the calculation of observables (e.g., to obtain the χ^2 in regard to experimental data), we use electromagnetic phase shifts (as necessary), which we obtain by

adding to the Coulomb phase shifts the effects from two-photon exchange, vacuum polarization, and magnetic moment interactions as calculated by the Nijmegen group [28, 35]. This is important for $^1S_0$ below 30 MeV and negligible otherwise. For nn and np scattering, our phase shifts are the ones from the nuclear interaction with respect to Riccati-Bessel functions. The technical details of our phase shift calculations can be found in Appendix A3 of Ref. [36].

The low-energy scattering parameters, order by order for the cutoff combination $(R_\pi, R_{\rm ct}) = (1.0, 0.70)$ fm, are shown in Table 3.2. For nn and np, the effective range expansion without any electromagnetic interaction is used. In the case of pp scattering, the quantities a_{pp}^C and r_{pp}^C are obtained by using the effective range expansion appropriate in the presence of the Coulomb force (cf. Appendix A4 of Ref. [36]). Note that the empirical values for a_{pp}^C and r_{pp}^C in Table 3.2 were obtained by subtracting from the corresponding electromagnetic values the effects due to two-photon exchange and vacuum polarization. Thus, the comparison between theory and experiment for these two quantities is conducted correctly. a_{nn}^N, and a_{np} are fitted, all other quantities are predictions. Note that the $^3S_1$ effective range parameters a_t and r_t are not fitted. But the deuteron binding energy is fitted (cf. next subsection) and that essentially fixes a_t and r_t.

3.2 The deuteron and triton

The evolution of the deuteron properties from LO to N^{3}LO of chiral EFT are shown in Table 3.3. In all cases, we fit the deuteron binding energy to its empirical value of 2.224575 MeV using the LO contact parameters. All other deuteron properties are predictions. At NLO, the empirical deuteron properties are already well reproduced.

At the bottom of Table 3.3, we also show the predictions for the triton binding as obtained in 34-channel charge-dependent Faddeev calculations using only 2NFs. The result is around 8.1 MeV at N^{3}LO. This contribution from the 2NF will require only a moderate 3NF. The relatively low deuteron D-state probabilities ($\approx 4\%$ at N^{3}LO) and the concomitant generous

Table 3.3: Two- and three-nucleon bound-state properties as predicted by NN potentials at various orders of chiral EFT applying the cutoff combination $(R_\pi, R_{\rm ct}) = (1.0, 0.70)$ fm. (Deuteron: Binding energy B_d, asymptotic S state A_S, asymptotic D/S state η, quadrupole moment Q, D-state probability P_D; the prediction for Q is without meson-exchange current contributions and relativistic corrections. Triton: Binding energy B_t.) B_d is fitted, all other quantities are predictions.

	LO	NLO	NNLO	N^{3}LO	Empirical[a]
Deuteron					
B_d (MeV)	2.224575	2.224575	2.224575	2.224575	2.224575(9)
A_S (fm$^{-1/2}$)	0.8613	0.8833	0.8836	0.8852	0.8846(9)
η	0.0254	0.0259	0.0252	0.0242	0.0256(4)
Q (fm^2)	0.264	0.284	0.274	0.260	0.2859(3)
P_D (%)	5.08	5.67	5.02	4.03	—
Triton					
B_t (MeV)	11.92	7.87	7.98	8.09	8.48

[a]See Table XVIII of Ref. [36] for references.

triton binding energy predictions are a reflection of the fact that our NN potentials have a weaker tensor force than commonly used local position-space potentials. This can also be seen in the predictions for the ϵ_1 mixing parameter that is a measure for the strength of the mixing of the $^3S_1$ and $^3D_1$ states due to the tensor force. Our predictions for ϵ_1 at NNLO and N^{3}LO are on the lower side for lab. energies above 100 MeV (Fig. 3.1). However, there is agreement with the GWU analysis [34] at 100 MeV. Note that the average relative momentum in nuclear matter at normal density is equivalent to $T_{\rm lab} \approx 50$ MeV. Thus, the properties of NN potentials for $T_{\rm lab} \lesssim 100$ MeV are the most important ones for nuclear structure applications. The discrepancies between the Nijmegen [30] and the GWU [34] analyses for ϵ_1 may be seen as an indication that this parameter is not as well determined as the uncertainties quoted in the various analyses suggest. The χ^2/datum of our N^{3}LO potential is 1.45, which is a typical value achieved in the GWU phase shift analysis. Thus, our N^{3}LO phase shift predictions, including the one for ϵ_1, is consistent with the NN data up to 190 MeV and may be viewed as an alternative phase shift analysis.

Table 3.4: χ^2/datum for the fit of the *pp* plus *np* data up to 100 MeV and two- and three-nucleon bound-state properties as produced by NN potentials at NNLO and N^{3}LO with the cutoff combinations $(R_\pi, R_{\rm ct}) = (1.2, 0.75)$ fm, $(1.1, 0.72)$ fm, and $(1.0, 0.70)$ fm. In the column headings, we use the R_π value to identify the different cases. For some of the notation, see Table 3.3, where also empirical information on the deuteron and triton can be found.

	NNLO			N^{3}LO		
	$R_\pi = 1.2$ fm	1.1 fm	1.0 fm	$R_\pi = 1.2$ fm	1.1 fm	1.0 fm
χ^2/datum *pp* & *np*						
0–100 MeV (1975 data)	2.75	2.39	2.45	1.75	1.56	1.48
Deuteron						
B_d (MeV)	2.224575	2.224575	2.224575	2.224575	2.224575	2.224575
A_S (fm$^{-1/2}$)	0.8862	0.8835	0.8836	0.8842	0.8851	0.8852
η	0.0244	0.0246	0.0252	0.0234	0.0239	0.0242
Q (fm^2)	0.263	0.265	0.274	0.248	0.255	0.260
P_D (%)	3.98	4.27	5.02	3.22	3.65	4.03
Triton						
B_t (MeV)	8.31	8.25	7.98	8.40	8.18	8.09

3.3 Cutoff variantions

As noted before, besides the cutoff combination $(R_\pi, R_{\rm ct}) = (1.0, 0.70)$ fm, we have also constructed potentials with the combinations (1.1, 0.72) fm, and (1.2, 0.75) fm, to allow for systematic studies of the cutoff dependence. In Fig. 3.2, we display the variations of the *np* phase shifts for different cutoffs at NNLO (left half of figure, green curves) and at N^{3}LO (right half of figure, red curves). Fig. 3.2 demonstrates nicely how cutoff dependence diminishes with increasing order—a reasonable trend. Another point that is evident from this figure is that (1.2, 0.75) fm should be considered as an upper limit for cutoffs, because obviously cutoff artifacts start showing up.

In Table 3.4, we show the cutoff dependence for three selected aspects that are of great interest: the χ^2 for the fit of the NN data below 100 MeV, the deuteron properties, and the triton binding energy. The χ^2 does not change substantially as a function of cutoff. Thus, we can make the interesting observation that the reproduction of NN observables is not much affected by the cutoff variations. However, the D-state probability of the deuteron, P_D,

which is not an observable, changes substantially as a function of cutoff. As discussed, P_D is intimately related to the strength of the tensor force of a potential and so are the binding energies of few-body systems. In particular, the cutoff combination $(R_\pi, R_{\rm ct}) = (1.1, 0.72)$ fm and (1.2, 0.75) fm at NNLO as well as N^{3}LO generate the substantial triton binding energies between 8.20 and 8.40 MeV and, therefore, differ significantly from other local position-space potentials that are commonly in use. On these grounds one can expect that results for light and intermediate-mass nuclei may differ considerably when applying our potentials in *ab initio* calculations. It will be interesting to see if this may solve some of the problems that some *ab initio* calculations with local potentials are currently beset with.

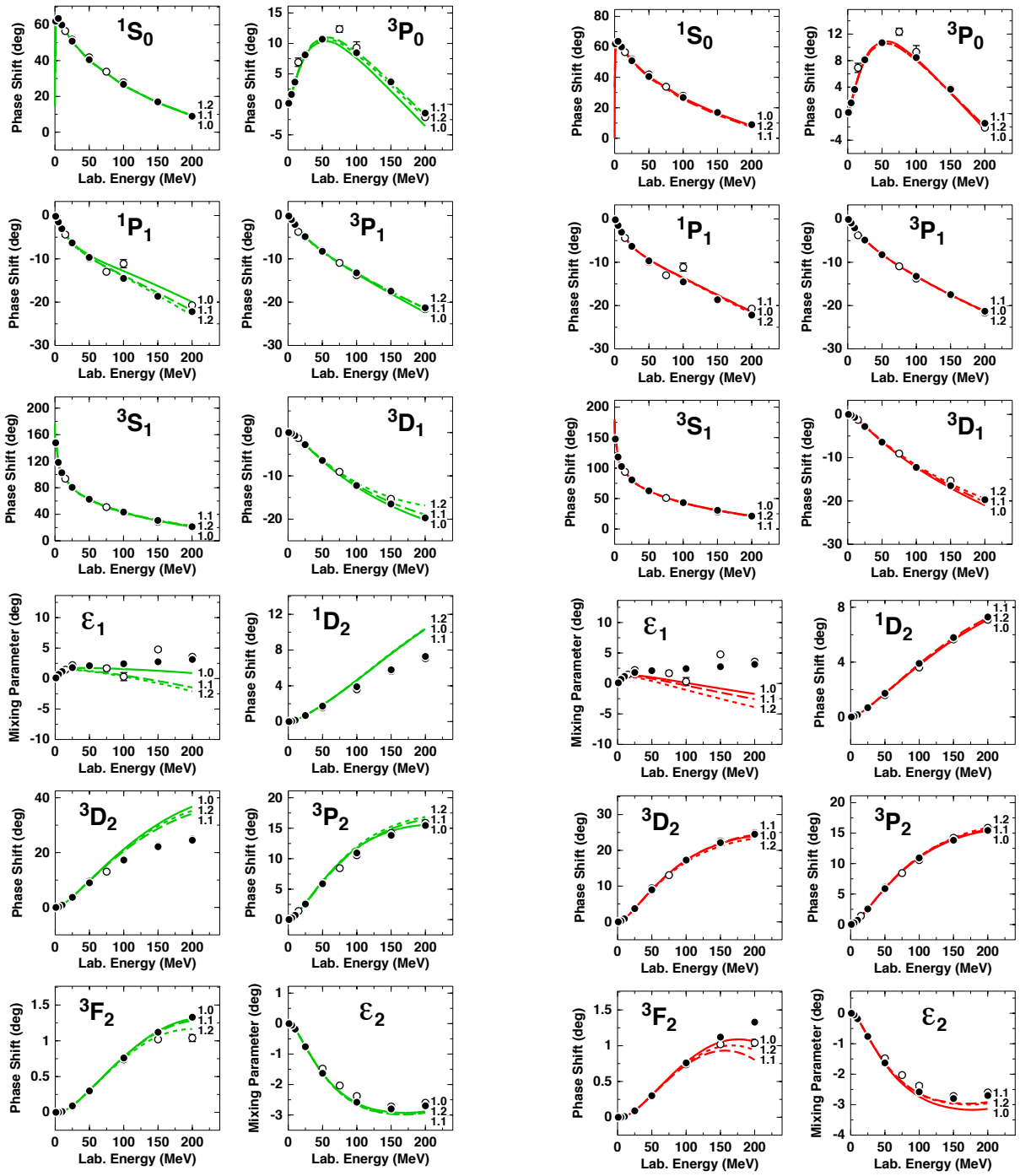

Figure 3.2: (Color online). Cutoff variations of the *np* phase shifts at NNLO (left side, green lines) and N^{3}LO (right side, red lines). Solid, dashed, and dotted lines represent the results obtained with the cutoff combinations $(R_\pi, R_{\rm ct})$ = (1.0, 0.70) fm, (1.1, 0.72) fm, and (1.2, 0.75) fm, respectively, as also indicated by the curve labels which state the R_π value. Filled and open circles as in Fig. 3.1.

CHAPTER 4

Uncertainty quantifications

In *ab initio* calculations applying chiral two- and many-body forces, major sources of uncertainties are [39]:

1. Experimental errors of the input NN data that the 2NFs are based upon and the input few-nucleon data to which the 3NFs are adjusted.

2. Uncertainties in the Hamiltonian due to

   (a) uncertainties in the determination of the NN and $3N$ contact LECs,

   (b) uncertainties in the πN LECs,

   (c) regulator dependence,

   (d) EFT truncation error.

3. Uncertainties associated with the few- and many-body methods applied.

The experimental errors in the NN scattering and deuteron data propagate into the NN potentials that are adjusted to reproduce those data. To systematically investigate this error propagation, the Granada group has constructed smooth local potentials [40], the parameters of which carry the uncertainties implied by the errors in the NN data. Applying 205 Monte Carlo samples of these potentials, they find an uncertainty of 15 keV for the triton binding energy [41]. In a more recent study [42], in which only 33 Monte Carlo samples were used, the Granada group reproduced the uncertainty of 15 keV for the triton binding energy and, in addition, determined the uncertainty for the ^{4}He binding energy to be 55 keV. The conclusion is that the statistical error propagation from the NN input data to the binding energies of light nuclei is negligible as compared to uncertainties from other sources (discussed below). Thus, this source of error can be safely neglected at this time. Furthermore, we need to consider the propagation of experimental errors from the experimental few-nucleon data that the 3NF contact terms are fitted to. Also this will be

negligible as long as the 3NFs are adjusted to data with very small experimental errors; for example the empirical binding energy of the triton is 8.481795 ± 0.000002 MeV, which will definitely lead to negligible propagation.

Now turning to the Hamiltoninan, we have to, first, account for uncertainties in the NN and $3N$ LECs due to the way they are fixed. Based upon our experiences from Ref. [43] and the fact that chiral EFT is a low-energy expansion, we have fitted the NN contact LECs to the NN data below 100 MeV at LO and NLO and below 190 MeV at NNLO and N^{3}LO. One could think of choosing these fit-intervals slightly different and a systematic investigation of the impact of such variation on the NN LECs is still outstanding. However, we do not anticipate that large uncertainties would emerge from this source of error.

The story is different for the 3NF contact LECs, since several, very different procedures are in use for how to fix them. The 3NF at NNLO has two free parameters (known as the c_D and c_E parameters). To fix them, two data are needed. In most procedures, one of them is the triton binding energy. For the second datum, the following choices have been made: the nd doublet scattering length ${}^2a_{nd}$ [44], the binding energy of ^{4}He [45], the point charge radius radius of ^{4}He [46], the Gamow-Teller matrix element of tritium β-decay [47, 48, 49]. Alternatively, the c_D and c_E parameters have also been pinned down by just an optimal over-all fit of the properties of light nuclei [50]. 3NF contact LECs determined by different procedures will lead to different predictions for the observables that were not involved in the fitting procedure. The differences in those results establish the uncertainty. Specifically, it would be of interest to investigate the differences that occur for the properties of intermediate-mass nuclei and nuclear matter when 3NF LECs fixed by different protocols are applied.

The uncertainty in the πN LECs used to be a large source of uncertainty, in particular, for predictions for many-body systems [51, 52, 53]. With the new, high-precision determination of the πN LECs in the Roy-Steiner equations analysis [21] (cf. Table 2.1) this large uncertainty is essentially eliminated, which is great progress, since it substantially reduces

the error budget. We have varied the πN LECs within the errors given in Table 2.1 and find that the changes caused by these variations can easily be compensated by small readjustments of the NN LECs resulting in essentially identical phase shifts and χ^2 for the fit of the data. Thus, this source of error is essentially negligible. The πN LECs also appear in the 3NFs, which also include contacts that can be used for readjustment. Future calculations of finite nuclei and nuclear matter should investigate what residual changes remain after such readjustment (that would represent the uncertainty). We expect this to be small.

The choice of the regulator function and its cutoff parameter create uncertainty. Originally, cutoff variations were perceived as a demonstration of the uncertainty at a given order (equivalent to the truncation error). However, in various investigations [18, 19] it has been demonstrated that this is not correct and that cutoff variations, in general, underestimate this uncertainty. Therefore, the truncation error is better determined by sticking literally to what 'truncation error' means, namely, the error due to omitting the contributions from orders beyond the given order ν. The largest such contribution is the one of order $(\nu+1)$, which one may, therefore, consider as representative for the magnitude of what is left out. This suggests that the truncation error at order ν can reasonably be defined as

$$\Delta X_\nu(p) = |X_\nu(p) - X_{\nu+1}(p)|\,, \tag{4.1}$$

where $X_\nu(p)$ denotes the prediction for observable X at order ν and momentum p. If $X_{\nu+1}$ is not available, then one may use,

$$\Delta X_\nu(p) = |X_{\nu-1}(p) - X_\nu(p)|Q\,, \tag{4.2}$$

with the expansion parameter Q chosen as

$$Q = \max\left\{\frac{m_\pi}{\Lambda_b},\ \frac{p}{\Lambda_b}\right\}\,, \tag{4.3}$$

where p is the characteristic center-of-mass (cms) momentum scale and Λ_b the breakdown scale.

Alternatively, one may also apply the more elaborate scheme suggested in Ref. [19] where the truncation error at, e.g., N^{3}LO is calculated in the following way:

$$\begin{aligned}\Delta X_{\mathrm{N^3LO}}(p) &= \max\Big\{Q^5\times\big|X_{\mathrm{LO}}(p)\big|,\;\; Q^3\times\big|X_{\mathrm{LO}}(p)-X_{\mathrm{NLO}}(p)\big|,\\ &\qquad Q^2\times\big|X_{\mathrm{NLO}}(p)-X_{\mathrm{NNLO}}(p)\big|,\;\; Q\times\big|X_{\mathrm{NNLO}}(p)-X_{\mathrm{N^3LO}}(p)\big|\Big\},\end{aligned} \tag{4.4}$$

with $X_{\mathrm{N^3LO}}(p)$ denoting the N^{3}LO prediction for observable $X(p)$, etc.

Note that one should not add up (in quadrature) the uncertainties due to regulator dependence and the truncation error, because they are not independent. In fact, it is appropriate to leave out the uncertainty due to regulator dependence entirely and just focus on the truncation error [19]. The latter should be estimated using the same cutoff in all orders considered.

Finally, the last uncertainty to be taken into account is the uncertainty in the few- and many-body methods applied in the *ab initio* calculation. This source of error has nothing to do with EFT. Few-body problems are nowadays exactly solvable such that the error is negligible in those cases. For heavier nuclei and nuclear matter, there are definitely uncertainties no matter what method is used. These uncertainties need to be estimated by the practitioners of those methods. But with the improvements of algoriths and the increase of computing power these errors are decreasing.

The bottom line is that the most substantial uncertainty is the truncation error. This is the dominant source of (systematic) error that should be carefully estimated for any calculation applying chiral 2NFs and 3NFs up to a given order.

CHAPTER 5

Summary and Conclusions

We have constructed local, position-space chiral NN potentials through four orders of chiral EFT ranging from LO to N^{3}LO. The construction may be perceived as consistent, because the same power counting scheme as well as the same cutoff procedures are applied in all orders. Moreover, the long-range parts of these potentials are fixed by the very accurate πN LECs as determined in the Roy-Steiner equations analysis of Ref. [21]. In fact, the uncertainties of these LECs are so small that a variation within the errors leads to effects that are essentially negligible at the current level of precision. Another aspect that has to do with precision is that, at least at the highest order (N^{3}LO), the NN data below 190 MeV laboratory energy are reproduced with the respectable χ^2/datum of 1.45.

The NN potentials presented in this thesis may serve as a solid basis for systematic *ab initio* calculations of nuclear structure and reactions that allow for a comprehensive error analysis. In particular, the order by order development of the potentials will make possible a reliable determination of the truncation error at each order.

Our new family of local position-space potentials differs from the already available potentials of this kind [9, 10, 11] by a weaker tensor force as reflected in relatively low D-state probabilities of the deuteron ($P_D \lesssim 4.0$ % for our N^{3}LO potentials) and predictions for the triton binding energy above 8.00 MeV (from two-body forces alone). As a consequence, our potentials will also lead to different predictions when applied to light and intermediate-mass nuclei in *ab initio* calculations. It will be interesting to see if this will help solving some of the outstanding problems in microscopic nuclear structure.

References

[1] S. Weinberg, Phys. Lett **B251**, 288 (1990); Nucl. Phys. **B363**, 3 (1991).

[2] R. Machleidt and D. R. Entem, Phys. Rep. **503**, 1 (2011).

[3] E. Epelbaum, H.-W. Hammer, and U.-G. Meißner, Rev. Mod. Phys. **81**, 1773 (2009).

[4] H.-W. Hammer, S. Kőnig, and U. van Kolck, Rev. Mod. Phys. **92**, 025004 (2020).

[5] K. Hebeler, Phys. Rept. **890**, 1 (2021).

[6] J. Carlson, S. Gandolfi, F. Pederiva, S. C. Pieper, R. Schiavilla, K. E. Schmidt, and R. B. Wiringa, Rev. Mod. Phys. **87**, 1067 (2015).

[7] J. E. Lynn, I. Tews, S. Gandolfi, and A. Lovato, Ann. Rev. Nucl. Part. Sci. **69**, 279-305 (2019).

[8] M. Piarulli and I. Tews, Front. in Phys. **7**, 245 (2020).

[9] A. Gezerlis, I. Tews, E. Epelbaum, M. Freunek, S. Gandolfi, K. Hebeler, A. Nogga, and A. Schwenk, Phys. Rev. C **90**, no.5, 054323 (2014).

[10] M. Piarulli, L. Girlanda, R. Schiavilla, R. Navarro Pérez, J. E. Amaro, and E. Ruiz Arriola, Phys. Rev. C **91**, no.2, 024003 (2015).

[11] M. Piarulli, L. Girlanda, R. Schiavilla, A. Kievsky, A. Lovato, L. E. Marcucci, S. C. Pieper, M. Viviani, and R. B. Wiringa, Phys. Rev. C **94**, no.5, 054007 (2016).

[12] Y. Nosyk, D. R. Entem, and R. Machleidt, Phys. Rev. C **104**, 054001 (2021).

[13] R. J. Furnstahl, N. Klco, D. R. Phillips, and S. Wesolowski, Phys. Rev. C **92**, 024005 (2015).

[14] N. Kaiser, Phys. Rev. C **61**, 014003 (2000).

[15] N. Kaiser, Phys. Rev. C **62**, 024001 (2000).

[16] D. R. Entem and R. Machleidt, Phys. Rev. C **66**, 014002 (2002).

[17] D. R. Entem and R. Machleidt, Phys. Rev. C **68**, 041001 (2003).

[18] F. Sammarruca, L. Coraggio, J. W. Holt, N. Itaco, R. Machleidt, and L. E. Marcucci, Phys. Rev. C **91**, 054311 (2015).

[19] E. Epelbaum, H. Krebs, and Ulf-G. Meißner, Eur. Phys. J. A **51**, 53 (2015).

[20] D. R. Entem, R. Machleidt, and Y. Nosyk, Phys. Rev. C **96**, 024004 (2017).

[21] M. Hoferichter, J. Ruiz de Elvira, B. Kubis, and U.-G. Meißner, Phys. Rev. Lett. **115**, 192301 (2015); Phys. Rep. **625**, 1 (2016).

[22] P.A. Zyla et al. (Particle Data Group), Prog. Theor. Exp. Phys. 2020, 083C01 (2020).

[23] S. Okubo and R. E. Marshak, Ann. Phys. (N.Y.) **4**, 166 (1958).

[24] M. Fierz, Z. Physik **104**, 553 (1937).

[25] L. Huth, I. Tews, J. E. Lynn, and A. Schwenk, Phys. Rev. C **96**, no.5, 054003 (2017).

[26] R. B. Wiringa, V. G. J. Stoks, and R. Schiavilla, Phys. Rev. C **51**, 38-51 (1995).

[27] G. J. M. Austin and J. J. de Swart, Phys. Rev. Lett. **50**, 2039 (1983).

[28] J. R. Bergervoet, P. C. van Campen, W. A. van der Sanden, and J. J. de Swart, Phys. Rev. C **38**, 15 (1988).

[29] U. van Kolck, M. C. M. Rentmeester, J. L. Friar, T. Goldman, and J. J. de Swart, Phys. Rev. Lett. **80**, 4386 (1998).

[30] V. G. J. Stoks, R. A. M. Klomp, M. C. M. Rentmeester, and J. J. de Swart, Phys. Rev. C **48**, 792 (1993).

[31] D. E. González Trotter *et al.*, Phys. Rev. C **73**, 034001 (2006).

[32] Q. Chen *et al.*, Phys. Rev. C **77**, 054002 (2008).

[33] R. Machleidt, K. Holinde, and Ch. Elster, Phys. Rep. **149**, 1 (1987).

[34] R. A. Arndt, W. J. Briscoe, I. I. Strakovsky, and R. L. Workman, Phys. Rev. C **76**, 025209 (2007).

[35] V. G. J. Stoks (private communication).

[36] R. Machleidt, Phys. Rev. C **63**, 024001 (2001).

[37] W. A. van der Sanden, A. H. Emmen, and J. J. de Swart, Report No. THEF-NYM-83.11, Nijmegen (1983), unpublished; quoted in Ref. [28].

[38] G. A. Miller, M. K. Nefkens, and I. Slaus, Phys. Rep. **194**, 1 (1990).

[39] R. J. Furnstahl, D. R. Phillips, and S. Wesolowski, J. Phys. G **42**, 034028 (2015).

[40] R. Navarro Perez, J. E. Amaro, and E. Ruiz Arriola, Phys. Rev. C **89**, 064006 (2014).

[41] R. Navarro Perez, E. Garrido, J. E. Amaro, and E. Ruiz Arriola, Phys. Rev. C **90**, 047001 (2014).

[42] R. Navarro Perez, J. E. Amaro, E. Ruiz Arriola, P. Maris, and J. P. Vary, Phys. Rev. C **92**, 064003 (2015).

[43] E. Marji *et al.*, Phys. Rev. C **88**, 054002 (2013).

[44] E. Epelbaum, A. Nogga, W. Gloeckle, H. Kamada, U. G. Meissner, and H. Witala, Phys. Rev. C **66**, 064001 (2002).

[45] A. Nogga, P. Navratil, B. R. Barrett, and J. P. Vary, Phys. Rev. C **73** (2006) 064002.

[46] K. Hebeler, S. K. Bogner, R. J. Furnstahl, A. Nogga, and A. Schwenk, Phys. Rev. C **83**, 031301(R) (2011).

[47] A. Gårdestig and D. R. Philips, Phys. Rev. Lett. **96** (2006) 232301.

[48] D. Gazit, S. Quaglioni, and P. Navrátil, Phys. Rev. Lett. **103** (2009) 102502.

[49] L. E. Marcucci, A. Kievsky, S. Rosati, R. Schiavilla, and M. Viviani, Phys. Rev. Lett. **108**, 052502 (2012).

[50] P. Navratil, V. G. Gueorguiev, J. P. Vary, W. E. Ormand, and A. Nogga, Phys. Rev. Lett. **99** (2007) 042501.

[51] T. Krűger, I. Tews, K. Hebeler, and A. Schwenk, Phys. Rev. C **88**, 025802 (2013).

[52] C. Drischler, K. Hebeler, and A. Schwenk, Phys. Rev. C **93**, 054314 (2016).

[53] C. Drischler, A. Carbone, K. Hebeler, and A. Schwenk, Phys. Rev. C **94**, 054307 (2016).

[54] V. Lapoux, V. Somà, C. Barbieri, H. Hergert, J. D. Holt, and S. R. Stroberg, Phys. Rev. Lett. **117**, 052501 (2016).

[55] S. Binder, J. Langhammer, A. Calci, and R. Roth, Phys. Lett. B **736**, 119 (2014).

[56] N. Kaiser, R. Brockmann, and W. Weise, Nucl. Phys. **A625**, 758 (1997).

[57] N. Kaiser, Phys. Rev. C **64**, 057001 (2001).

[58] D. R. Entem, N. Kaiser, R. Machleidt, and Y. Nosyk, Phys. Rev. C **91**, 014002 (2015).

APPENDIX A

The long-range NN potential

For each order, we will state, first, the momentum-space functions and then the corresponding position-space potentials as obtained by Fourier transform. Note that all long-range potentials are local.

In momentum space, we use the following notation for the decomposition of the long-range potential,

$$\begin{aligned} V_\pi(\vec{p}\,',\vec{p}) \;=\;& V_C(q) \;+\boldsymbol{\tau}_1\cdot\boldsymbol{\tau}_2\, W_C(q) \\ &+[\,V_S(q) \;+\boldsymbol{\tau}_1\cdot\boldsymbol{\tau}_2\, W_S(q)\;]\;\vec{\sigma}_1\cdot\vec{\sigma}_2 \\ &+[\,V_T(q) \;+\boldsymbol{\tau}_1\cdot\boldsymbol{\tau}_2\, W_T(q)\;]\;\vec{\sigma}_1\cdot\vec{q}\;\vec{\sigma}_2\cdot\vec{q} \\ &+[\,V_{LS}(q)+\boldsymbol{\tau}_1\cdot\boldsymbol{\tau}_2\, W_{LS}(q)]\left(-i\vec{S}\cdot(\vec{q}\times\vec{k})\right). \end{aligned} \tag{A.1}$$

For notation, see Sec. 2.4. The position-space potential is represented as follows:

$$\begin{aligned} \widetilde{V}_\pi(\vec{r}) \;=\;& \widetilde{V}_C(r) \;+\boldsymbol{\tau}_1\cdot\boldsymbol{\tau}_2\,\widetilde{W}_C(r) \\ &+\left[\,\widetilde{V}_S(r) \;+\boldsymbol{\tau}_1\cdot\boldsymbol{\tau}_2\,\widetilde{W}_S(r)\;\right]\vec{\sigma}_1\cdot\vec{\sigma}_2 \\ &+\left[\,\widetilde{V}_T(r) \;+\boldsymbol{\tau}_1\cdot\boldsymbol{\tau}_2\,\widetilde{W}_T(r)\;\right]S_{12}(\hat{r}) \\ &+\left[\,\widetilde{V}_{LS}(r)+\boldsymbol{\tau}_1\cdot\boldsymbol{\tau}_2\,\widetilde{W}_{LS}(r)\right]\vec{L}\cdot\vec{S}\,, \end{aligned} \tag{A.2}$$

where the operator for total orbital angular momentum is denoted by $\vec{L}$.

The 2PE potentials in spectral representation are given in momentum space by

$$\begin{aligned} V_{C,S}(q) &= -\frac{2q^6}{\pi}\int_{2m_\pi}^{\infty} d\mu \frac{\mathrm{Im}V_{C,S}(i\mu)}{\mu^5(\mu^2+q^2)}\,, \\ V_{T,LS}(q) &= \frac{2q^4}{\pi}\int_{2m_\pi}^{\infty} d\mu \frac{\mathrm{Im}V_{T,LS}(i\mu)}{\mu^3(\mu^2+q^2)}\,, \end{aligned} \tag{A.3}$$

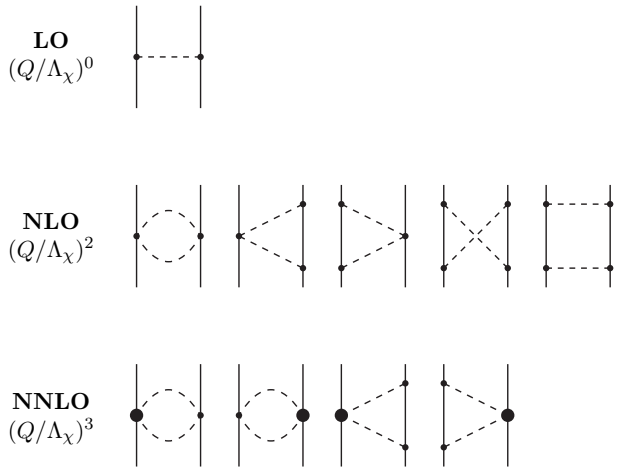

Figure A.1: LO, NLO, and NNLO pion-exchange contributions to the NN interaction. Notation as in Fig. 2.1.

and similarly for $W_{C,S,T,LS}$. Their Fourier transforms are

$$\begin{aligned}
\widetilde{V}_C(r) &= \frac{1}{2\pi^2 r}\int_{2m_\pi}^{\infty} d\mu\mu e^{-\mu r}\mathrm{Im}V_C(i\mu)\,, \\
\widetilde{V}_S(r) &= -\frac{1}{6\pi^2 r}\int_{2m_\pi}^{\infty} d\mu\mu e^{-\mu r}\left[\mu^2\mathrm{Im}V_T(i\mu) - 3\mathrm{Im}V_S(i\mu)\right]\,, \\
\widetilde{V}_T(r) &= -\frac{1}{6\pi^2 r^3}\int_{2m_\pi}^{\infty} d\mu\mu e^{-\mu r}(3+3\mu r+\mu^2 r^2)\mathrm{Im}V_T(i\mu)\,, \\
\widetilde{V}_{LS}(r) &= \frac{1}{2\pi^2 r^3}\int_{2m_\pi}^{\infty} d\mu\mu e^{-\mu r}(1+\mu r)\mathrm{Im}V_{LS}(i\mu)\,,
\end{aligned} \tag{A.4}$$

and similarly for $\widetilde{W}_{C,S,T,LS}$.

A.1 Leading order

At leading order, only 1PE contributes to the long range, cf. Fig. A.1. The charge-independent 1PE is given in momentum space by

$$W_T(q) = -\frac{g_A^2}{4f_\pi^2}\,\frac{1}{q^2+m_\pi^2}\,, \tag{A.5}$$

where g_A, f_π, and m_π denote the axial-vector coupling constant, pion-decay constant, and the pion mass, respectively. See Table 2.2 for their values. Fourier transform yields:

$$\widetilde{W}_S(r) = \frac{g_A^2 m_\pi^2}{48\pi f_\pi^2}\,\frac{e^{-x}}{r}\,, \tag{A.6}$$

$$\widetilde{W}_T(r) = \frac{g_A^2}{48\pi f_\pi^2}\,\frac{e^{-x}}{r^3}(3+3x+x^2)\,, \tag{A.7}$$

with $x = m_\pi r$.

For the NN potentials constructed in this thesis, we take the charge-dependence of the 1PE due to pion-mass splitting into account. For this, we define:

$$\widetilde{V}_S(m_\pi) = \frac{g_A^2 m_\pi^2}{48\pi f_\pi^2}\,\frac{e^{-x}}{r}\,, \tag{A.8}$$

$$\widetilde{V}_T(m_\pi) = \frac{g_A^2}{48\pi f_\pi^2}\,\frac{e^{-x}}{r^3}(3+3x+x^2)\,. \tag{A.9}$$

The proton-proton (pp) and neutron-neutron (nn) potentials are then given by:

$$\widetilde{V}_S^{(pp)}(r) = \widetilde{V}_S^{(nn)}(r) = \widetilde{V}_S(m_{\pi^0})\,, \tag{A.10}$$

$$\widetilde{V}_T^{(pp)}(r) = \widetilde{V}_T^{(nn)}(r) = \widetilde{V}_T(m_{\pi^0})\,, \tag{A.11}$$

and the neutron-proton (np) potentials are:

$$\widetilde{V}_S^{(np)}(r) = -\widetilde{V}_S(m_{\pi^0}) + (-1)^{T+1}\,2\,\widetilde{V}_S(m_{\pi^\pm})\,, \tag{A.12}$$

$$\widetilde{V}_T^{(np)}(r) = -\widetilde{V}_T(m_{\pi^0}) + (-1)^{T+1}\,2\,\widetilde{V}_T(m_{\pi^\pm})\,, \tag{A.13}$$

where $T = 0, 1$ denotes the total isospin of the two-nucleon system. See Table 2.2 for the precise values of the pion masses. Formally speaking, the charge-dependence of the 1PE exchange is of order NLO [2], but we include it also at leading order to make the comparison with the (charge-dependent) phase-shift analyses meaningful.

A.2 Next-to-leading order

The 2PE NN diagrams that occur at NLO (cf. Fig. A.1) contribute—in momentum space—in the following way [56]:

$$W_C(q) = \frac{L(q)}{384\pi^2 f_\pi^4}\left[4m_\pi^2(1+4g_A^2-5g_A^4)+q^2(1+10g_A^2-23g_A^4)-\frac{48g_A^4m_\pi^4}{w^2}\right], \quad (A.14)$$

$$V_T(q) = -\frac{1}{q^2}V_S(q) = -\frac{3g_A^4}{64\pi^2 f_\pi^4}L(q)\,, \quad (A.15)$$

with the logarithmic loop function

$$L(q) = \frac{w}{q}\ln\frac{w+q}{2m_\pi} \quad (A.16)$$

and $w=\sqrt{4m_\pi^2+q^2}$. Note that we apply dimensional renormalization for all loop diagrams. Moreover, in all 2PE contributions, we use the average pion-mass, i. e., $m_\pi = \bar{m}_\pi$ (cf. Table 2.2).

These expressions imply the spectral functions

$$\begin{aligned}\mathrm{Im}W_C(i\mu) &= -\frac{1}{768\pi f_\pi^4}\frac{\sqrt{\mu^2-4m_\pi^2}}{\mu}\Bigg[4m_\pi^2(1+4g_A^2-5g_A^4)\\ &\quad -\mu^2(1+10g_A^2-23g_A^4)-\frac{48g_A^4m_\pi^4}{4m_\pi^2-\mu^2}\Bigg], \quad (A.17)\\ \mathrm{Im}V_T(i\mu) &= \frac{1}{\mu^2}\mathrm{Im}V_S(i\mu) = \frac{3g_A^4}{128\pi f_\pi^4}\frac{\sqrt{\mu^2-4m_\pi^2}}{\mu}\,. \quad (A.18)\end{aligned}$$

Via Fourier transform, Eq. (A.4), the equivalent position-space potentials are:

$$\begin{aligned}
\widetilde{W}_C(r) &= \frac{m_\pi}{128\pi^3 f_\pi^4}\frac{1}{r^4}\Big\{\left[1+2g_A^2(5+2x^2)-g_A^4(23+12x^2)\right]K_1(2x) \\
&\quad +x\left[1+10g_A^2-g_A^4(23+4x^2)\right]K_0(2x)\Big\}\,, \qquad \text{(A.19)} \\
\widetilde{V}_S(r) &= \frac{g_A^4 m_\pi}{32\pi^3 f_\pi^4}\frac{1}{r^4}\left[3xK_0(2x)+(3+2x^2)K_1(2x)\right]\,, \qquad \text{(A.20)} \\
\widetilde{V}_T(r) &= -\frac{g_A^4 m_\pi}{128\pi^3 f_\pi^4}\frac{1}{r^4}\left[12xK_0(2x)+(15+4x^2)K_1(2x)\right]\,, \qquad \text{(A.21)}
\end{aligned}$$

where K_0 and K_1 denote the modified Bessel functions.

A.3 Next-to-next-to-leading order

The 2PE NNLO contribution (cf. Fig. A.1) is given by [56]:

$$\begin{aligned}
V_C &= \frac{3g_A^2}{16\pi f_\pi^4}\left[2m_\pi^2(c_3-2c_1)+c_3q^2\right](2m_\pi^2+q^2)A(q)\,, \qquad \text{(A.22)} \\
W_T &= -\frac{1}{q^2}W_S = -\frac{g_A^2}{32\pi f_\pi^4}c_4 w^2 A(q)\,, \qquad \text{(A.23)}
\end{aligned}$$

with the loop function

$$A(q) = \frac{1}{2q}\arctan\frac{q}{2m_\pi}\,. \qquad \text{(A.24)}$$

The associated spectral functions are

$$\begin{aligned}
\mathrm{Im}V_C(i\mu) &= \frac{3g_A^2}{64\mu f_\pi^4}\left[2m_\pi^2(c_3-2c_1)-c_3\mu^2\right](2m_\pi^2-\mu^2)\,, \qquad \text{(A.25)} \\
\mathrm{Im}W_T(i\mu) &= \frac{1}{\mu^2}\mathrm{Im}W_S(i\mu) = -\frac{g_A^2}{128\mu f_\pi^4}c_4(4m_\pi^2-\mu^2)\,; \qquad \text{(A.26)}
\end{aligned}$$

which, by way of Eq. (A.4), yield the position-space expressions

$$\widetilde{V}_C(r) = \frac{3g_A^2}{32\pi^2 f_\pi^4}\frac{e^{-2x}}{r^6}\left[2c_1x^2(1+x)^2 + c_3(6+12x+10x^2+4x^3+x^4)\right] , \quad \text{(A.27)}$$

$$\widetilde{W_S}(r) = \frac{g_A^2}{48\pi^2 f_\pi^4}\frac{e^{-2x}}{r^6}c_4(1+x)(3+3x+2x^2) , \quad \text{(A.28)}$$

$$\widetilde{W_T}(r) = -\frac{g_A^2}{48\pi^2 f_\pi^4}\frac{e^{-2x}}{r^6}c_4(1+x)(3+3x+x^2) . \quad \text{(A.29)}$$

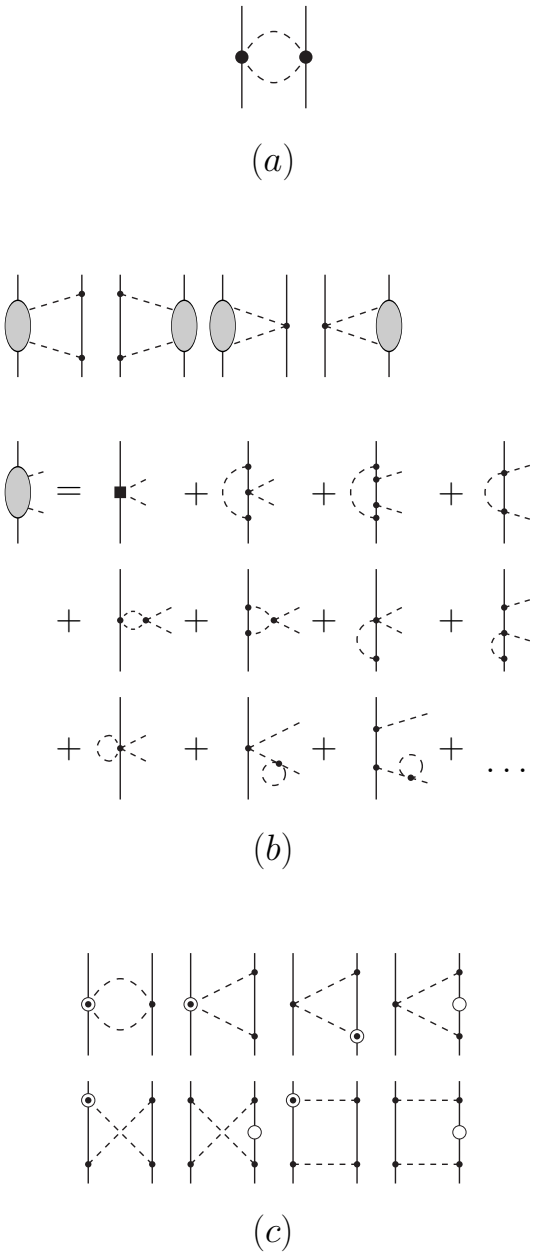

Figure A.2: Two-pion exchange contributions at N^{3}LO with (a) the N^{3}LO football diagram, (b) the leading 2PE two-loop contributions, and (c) the leading relativistic corrections. Basic notation as in Fig. 2.1. The shaded disc stands for all one-loop πN graphs as illustrated. Open circles are relativistic $1/M_N$ corrections.

A.4 Next-to-next-to-next-to-leading order

A.4.1 Football diagram at N^{3}LO

The N^{3}LO football diagram, Fig. A.2(a), generates [57]:

Momentum-space potentials:

$$V_C(q) = \frac{3\,L(q)}{16\pi^2 f_\pi^4}\left[\left(\frac{c_2}{6}w^2 + c_3(2m_\pi^2+q^2) - 4c_1 m_\pi^2\right)^2 + \frac{c_2^2}{45}w^4\right], \quad \text{(A.30)}$$

$$W_T(q) = -\frac{1}{q^2}W_S(q) = \frac{c_4^2\, w^2\, L(q)}{96\,\pi^2 f_\pi^4}\,. \quad \text{(A.31)}$$

Spectral functions:

$$\mathrm{Im}V_C(i\mu) = -\frac{3}{32\pi f_\pi^4}\frac{\sqrt{\mu^2-4m_\pi^2}}{\mu}\left[\left(\frac{c_2}{6}(4m_\pi^2-\mu^2) + c_3(2m_\pi^2-\mu^2) - 4c_1 m_\pi^2\right)^2 + \frac{c_2^2}{45}(4m_\pi^2-\mu^2)^2\right], \quad \text{(A.32)}$$

$$\mathrm{Im}W_T(i\mu) = \frac{1}{\mu^2}\mathrm{Im}W_S(i\mu) = \frac{c_4^2}{192\pi f_\pi^4}\frac{(\mu^2-4m_\pi^2)^{3/2}}{\mu}\,. \quad \text{(A.33)}$$

Position-space potentials:

$$\widetilde{V}_C(r) = -\frac{3m_\pi^7}{32\pi^3 f_\pi^4}\frac{1}{x^5}\Big[\left(3c_2^2+20c_2c_3+60c_3^2+4(2c_1+c_3)^2x^2\right)xK_1(2x) + 2\Big(3c_2^2+20c_2c_3+60c_3^2+2(2c_1+c_3) \times(c_2+6c_3)x^2\Big)K_2(2x)\Big], \quad \text{(A.34)}$$

$$\widetilde{W}_S(r) = \frac{c_4^2 m_\pi^7}{24\pi^3 f_\pi^4}\frac{1}{x^4}\Big[2xK_2(2x)+5K_3(2x)\Big], \quad \text{(A.35)}$$

$$\widetilde{W}_T(r) = -\frac{c_4^2 m_\pi^7}{96\pi^3 f_\pi^4}\frac{1}{x^5}\Big[(3+4x^2)K_2(2x)+16xK_3(2x)\Big], \quad \text{(A.36)}$$

where $K_2(z) = K_0(z) + \frac{2}{z}K_1(z)$ and $K_3(z) = K_1(z) + \frac{4}{z}K_2(z) = \frac{4}{z}K_0(z) + (\frac{8}{z^2}+1)K_1(z)$.

A.4.2 Leading 2PE two-loop diagrams

The leading-order 2π-exchange two-loop diagrams are shown in Fig. A.2(b). The various contributions are [57]:

Isoscalar central potential:

Spectral functions:

$$\begin{aligned}
\mathrm{Im}V_C^{(a)}(i\mu) &= -\frac{3g_A^4(\mu^2-2m_\pi^2)}{\pi\mu(4f_\pi)^6}\Big\{(m_\pi^2-2\mu^2)2m_\pi \\
&\quad +4g_A^2 m_\pi(2m_\pi^2-\mu^2)\Big\}\,, \qquad \text{(A.37)}\\
\mathrm{Im}V_C^{(b)}(i\mu) &= -\frac{3g_A^4(\mu^2-2m_\pi^2)}{\pi\mu(4f_\pi)^6}(m_\pi^2-2\mu^2)\frac{2m_\pi^2-\mu^2}{2\mu}\ln\frac{\mu+2m_\pi}{\mu-2m_\pi}\,. \qquad \text{(A.38)}
\end{aligned}$$

Position-space potentials:

$$\begin{aligned}
\widetilde{V}_C^{(a)}(r) &= \frac{3m_\pi^7 g_A^4}{2048\pi^3 f_\pi^6}\frac{e^{-2x}}{x^6}\Big\{24+48x+43x^2+22x^3+7x^4 \\
&\quad +4g_A^2(6+12x+10x^2+4x^3+x^4)\Big\}\,, \qquad \text{(A.39)}\\
\widetilde{V}_C^{(b)}(r) &= -\frac{3m_\pi^7 g_A^4}{8192\pi^3 f_\pi^6}\frac{e^{-2x}}{x^7}\Big\{(120+240x+213x^2 \\
&\quad +106x^3+32x^4+8x^5)(\ln(4x)+\gamma_E) \\
&\quad -(120-240x+213x^2-106x^3+32x^4-8x^5)e^{4x}\mathrm{Ei}(-4x) \\
&\quad -4x(96+72x+38x^2+7x^3)\Big\} \\
&\quad +\frac{3m_\pi^7 g_A^4}{4096\pi^3 f_\pi^6}\frac{\bar{I}_{-1}(2x)}{x}\,, \qquad \text{(A.40)}
\end{aligned}$$

where $\mathrm{Ei}(-z)$ denotes the exponential integral function defined by

$$\mathrm{Ei}(-z) = -\int_z^\infty dt\,\frac{e^{-t}}{t}\,, \qquad \text{(A.41)}$$

and

$$\bar{I}_{-1}(z) = \int_1^\infty dt\frac{e^{-zt}}{t}\ln\left(\frac{t+1}{t-1}\right). \qquad \text{(A.42)}$$

The double precision value for Euler's constant is $\gamma_E = 0.5772156649015329$.

Isovector central potential:

Spectral functions:

$$\begin{aligned}
\mathrm{Im}W_C^{(a)}(i\mu) &= -\frac{2\kappa}{3\mu(8\pi f_\pi^2)^3}\int_0^1 dz\left[g_A^2(2m_\pi^2-\mu^2)+2(g_A^2-1)\kappa^2z^2\right] \\
&\quad\times\Bigg\{\left[4m_\pi^2(1+2g_A^2)-\mu^2(1+5g_A^2)\right]\frac{\kappa}{\mu}\ln\frac{\mu+2\kappa}{2m_\pi}+\frac{\mu^2}{12}(5+13g_A^2) \\
&\quad -2m_\pi^2(1+2g_A^2)+96\pi^2f_\pi^2\left[(2m_\pi^2-\mu^2)(\bar{d}_1+\bar{d}_2)-2\kappa^2z^2\bar{d}_3+4m_\pi^2\bar{d}_5\right]\Bigg\} \\
&= -\frac{2\kappa}{3\mu(8\pi f_\pi^2)^3}\left[g_A^2(2m_\pi^2-\mu^2)+\frac{2}{3}(g_A^2-1)\kappa^2\right] \\
&\quad\times\Bigg\{\left[4m_\pi^2(1+2g_A^2)-\mu^2(1+5g_A^2)\right]\frac{\kappa}{\mu}\ln\frac{\mu+2\kappa}{2m_\pi}+\frac{\mu^2}{12}(5+13g_A^2) \\
&\quad -2m_\pi^2(1+2g_A^2)+96\pi^2f_\pi^2\left[(2m_\pi^2-\mu^2)(\bar{d}_1+\bar{d}_2)+4m_\pi^2\bar{d}_5\right]\Bigg\} \\
&\quad -\frac{\kappa^3}{\mu 4\pi f_\pi^4}\left[\frac{1}{3}g_A^2(2m_\pi^2-\mu^2)+\frac{2}{5}(g_A^2-1)\kappa^2\right]\bar{d}_3\,, \qquad \text{(A.43)}
\end{aligned}$$

$$\begin{aligned}
\mathrm{Im}W_C^{(b)}(i\mu) &= -\frac{2\kappa}{3\mu(8\pi f_\pi^2)^3}\int_0^1 dz\left[g_A^2(2m_\pi^2-\mu^2)+2(g_A^2-1)\kappa^2z^2\right] \\
&\quad\times\Bigg\{-3\kappa^2z^2+6\kappa z\sqrt{m_\pi^2+\kappa^2z^2}\ln\frac{\kappa z+\sqrt{m_\pi^2+\kappa^2z^2}}{m_\pi}+ \\
&\quad g_A^4(\mu^2-2\kappa^2z^2-2m_\pi^2)\Bigg[\frac{5}{6}+\frac{m_\pi^2}{\kappa^2z^2}-\left(1+\frac{m_\pi^2}{\kappa^2z^2}\right)^{3/2} \\
&\quad\times\ln\frac{\kappa z+\sqrt{m_\pi^2+\kappa^2z^2}}{m_\pi}\Bigg]\Bigg\}\,, \qquad \text{(A.44)}
\end{aligned}$$

with $\kappa = \sqrt{\mu^2/4 - m_\pi^2}$.

In Ref. [16] it was found that the contribution from $W_C^{(b)}$ is negligible. Therefore, we

include only $W_C^{(a)}$, which we divide it into three parts:

$$\begin{aligned}
\mathrm{Im}W_C^{(a_1)}(i\mu) &= -\frac{2\kappa}{3\mu(8\pi f_\pi^2)^3}\left[g_A^2(2m_\pi^2-\mu^2)+\frac{2}{3}(g_A^2-1)\kappa^2\right] \\
&\quad\times\left[4m_\pi^2(1+2g_A^2)-\mu^2(1+5g_A^2)\right]\frac{\kappa}{\mu}\ln\frac{\mu+2\kappa}{2m_\pi}\,, \qquad \text{(A.45)}\\
\mathrm{Im}W_C^{(a_2)}(i\mu) &= -\frac{2\kappa}{3\mu(8\pi f_\pi^2)^3}\left[g_A^2(2m_\pi^2-\mu^2)+\frac{2}{3}(g_A^2-1)\kappa^2\right] \\
&\quad\times\left\{\frac{\mu^2}{12}(5+13g_A^2)-2m_\pi^2(1+2g_A^2)+96\pi^2 f_\pi^2\left[(2m_\pi^2-\mu^2)\right.\right. \\
&\quad\left.\left.\times(\bar{d}_1+\bar{d}_2)+4m_\pi^2\bar{d}_5\right]\right\}, \qquad \text{(A.46)}\\
\mathrm{Im}W_C^{(a_3)}(i\mu) &= \frac{\kappa^3}{\mu 4\pi f_\pi^4}\left[\frac{1}{3}g_A^2(2m_\pi^2-\mu^2)+\frac{2}{5}(g_A^2-1)\kappa^2\right]\bar{d}_3\,, \qquad \text{(A.47)}
\end{aligned}$$

Position-space potentials:

$$\begin{aligned}
\widetilde{W}_C^{(a_1)}(r) &= -\frac{m_\pi^7}{9216\pi^5 f_\pi^6}\frac{1}{x^7}\left\{\left[30+89x^2-8x^4+g_A^2(300+926x^2-32x^4)\right.\right. \\
&\quad\left.+g_A^4(750+2405x^2+76x^4)\right]K_0(2x)+\left[137+8x^2+8x^4\right. \\
&\quad+2g_A^2(685+106x^2+16x^4)+g_A^4(3425+860x^2 \\
&\quad\left.\left.+32x^4)\right]xK_1(2x)\right\}+\frac{m_\pi^7}{576\pi^5 f_\pi^6}(1+2g_A^2)^2\frac{\widetilde{I}_{-1}(2x)}{x}\,, \qquad \text{(A.48)}\\
\widetilde{W}_C^{(a_2)}(r) &= -\frac{m_\pi^7}{8\pi^3 f_\pi^4}\left\{-\frac{2g_A^2xK_1(2x)+(1+5g_A^2)K_2(2x)}{x^3}2\bar{d}_5\right. \\
&\quad+\frac{(5+g_A^2(25+2x^2))xK_1(2x)+(10+x^2+g_A^2(50+11x^2))K_2(2x)}{x^5} \\
&\quad\left.\times(\bar{d}_1+\bar{d}_2)\right\}+\frac{m_\pi^7}{9216\pi^5 f_\pi^6}\frac{1}{x^5}\left\{(25+g_A^2(190-4x^2)\right. \\
&\quad+g_A^4(325+4x^2))xK_1(2x)+2(25-x^2+g_A^2(190+11x^2) \\
&\quad\left.+g_A^4(325+44x^2))K_2(2x)\right\}, \qquad \text{(A.49)}\\
\widetilde{W}_C^{(a_3)}(r) &= -\frac{m_\pi^7}{16\pi^3 f_\pi^4}\frac{2g_A^2xK_2(2x)+(3+7g_A^2)K_3(2x)}{x^4}\bar{d}_3\,, \qquad \text{(A.50)}
\end{aligned}$$

with

$$\widetilde{I}_{-1}(z)=\int_1^\infty dt\,\frac{e^{-zt}}{t}\ln(t+\sqrt{t^2-1}) \qquad \text{(A.51)}$$

Isoscalar spin-spin and tensor potentials:

Spectral functions:

$$\begin{aligned}
\mathrm{Im}V_S^{(a)}(i\mu) &= \mu^2\,\mathrm{Im}V_T^{(a)}(i\mu) = -\frac{g_A^2\kappa^3\mu}{8\pi f_\pi^4}(\bar{d}_{14}-\bar{d}_{15})\,, && \text{(A.52)}\\
\mathrm{Im}V_S^{(b)}(i\mu) &= \mu^2\,\mathrm{Im}V_T^{(b)}(i\mu) \\
&= -\frac{2g_A^6\kappa^3\mu}{(8\pi f_\pi^2)^3}\int_0^1 dz(1-z^2)\Big[-\frac{1}{6}+\frac{m_\pi^2}{\kappa^2 z^2} \\
&\quad -\left(1+\frac{m_\pi^2}{\kappa^2 z^2}\right)^{3/2}\ln\frac{\kappa z+\sqrt{m_\pi^2+\kappa^2 z^2}}{m_\pi}\Big]\,. && \text{(A.53)}
\end{aligned}$$

In Ref. [16] it was found that the contribution from $V_S^{(b)}$ and $V_T^{(b)}$ are negligible. Therefore, we include only $V_S^{(a)}$ and $V_T^{(a)}$, which yield the position-space potentials:

$$\begin{aligned}
\widetilde{V}_S^{(a)}(r) &= -\frac{g_A^2 m_\pi^7}{8\pi^3 f_\pi^4 x^4}(\bar{d}_{14}-\bar{d}_{15})(2xK_2(2x)+5K_3(2x))\,, && \text{(A.54)}\\
\widetilde{V}_T^{(a)}(r) &= \frac{g_A^2 m_\pi^7}{32\pi^3 f_\pi^4 x^5}(\bar{d}_{14}-\bar{d}_{15})\left[(3+4x^2)K_2(2x)+16xK_3(2x)\right]\,. && \text{(A.55)}
\end{aligned}$$

Isovector spin-spin and tensor potentials:

Spectral functions:

$$\begin{aligned}
\mathrm{Im}W_S(i\mu) &= -\frac{g_A^4(\mu^2-4m_\pi^2)}{\pi(4f_\pi)^6}\Bigg\{\left[m_\pi^2-\frac{\mu^2}{4}\right]\ln\left(\frac{\mu+2m_\pi}{\mu-2m_\pi}\right) \\
&\quad +(1+2g_A^2)\mu m_\pi\Bigg\}\,, \qquad \text{(A.56)} \\
\mathrm{Im}W_T^{(a)}(i\mu) &= -\frac{1}{\mu^2}\frac{g_A^4(\mu^2-4m_\pi^2)}{\pi(4f_\pi)^6}(1+2g_A^2)\mu m_\pi\,, \qquad \text{(A.57)} \\
\mathrm{Im}W_T^{(b)}(i\mu) &= -\frac{1}{\mu^2}\frac{g_A^4(\mu^2-4m_\pi^2)}{\pi(4f_\pi)^6}\left[m_\pi^2-\frac{\mu^2}{4}\right]\ln\left(\frac{\mu+2m_\pi}{\mu-2m_\pi}\right). \qquad \text{(A.58)}
\end{aligned}$$

Position-space potentials:

$$\begin{aligned}
\widetilde{W}_S(r) &= \frac{g_A^4 m_\pi^7}{6144\pi^3 f_\pi^6}\frac{e^{-2x}}{x^7}\Bigg\{(15+30x+24x^2+8x^3)(\ln(4x)+\gamma_E) \\
&\quad +(-15+30x-24x^2+8x^3)e^{4x}\mathrm{Ei}(-4x) \\
&\quad -4x(15+15x+8x^2+2x^3) \\
&\quad -8g_A^2x(3+6x+5x^2+2x^3)\Bigg\}\,, \qquad \text{(A.59)} \\
\widetilde{W}_T^{(a)}(r) &= \frac{g_A^4(1+2g_A^2)m_\pi^7}{1536\pi^3 f_\pi^6}\frac{e^{-2x}}{x^6}(3+6x+4x^2+x^3)\,, \qquad \text{(A.60)} \\
\widetilde{W}_T^{(b)}(r) &= -\frac{g_A^4 m_\pi^7}{49152\pi^3 f_\pi^6}\frac{e^{-2x}}{x^7}\Bigg\{-324x-228x^2-48x^3 \\
&\quad +5(21+42x+30x^2+4x^3)(\ln(4x)+\gamma_E) \\
&\quad +5(-21+42x-30x^2+4x^3)e^{4x}\mathrm{Ei}(-4x)\Bigg\} \\
&\quad -\frac{g_A^4 m_\pi^7}{2048\pi^3 f_\pi^6}\frac{1}{x^3}\bar{I}_{-1}(2x)\,. \qquad \text{(A.61)}
\end{aligned}$$

A.4.3 Leading relativistic corrections

The leading relativistic corrections, which are shown in Fig. A.2(c), count as $\mathrm{N^3LO}$ and are given by [58]:

Momentum-space potentials:

$$V_C(q) = \frac{3g_A^4}{128\pi f_\pi^4 M_N}\left[\frac{m_\pi^5}{2w^2} + (2m_\pi^2+q^2) \times(q^2-m_\pi^2)A(q)\right], \quad \text{(A.62)}$$

$$W_C(q) = \frac{g_A^2}{64\pi f_\pi^4 M_N}\left\{\frac{3g_A^2 m_\pi^5}{2w^2} + \left[(g_A^2(3m_\pi^2+2q^2) -q^2-2m_\pi^2\right](2m_\pi^2+q^2)A(q)\right\}, \quad \text{(A.63)}$$

$$V_T(q) = -\frac{1}{q^2}V_S(q) = \frac{3g_A^4}{256\pi f_\pi^4 M_N}(5m_\pi^2+2q^2)A(q)\,, \quad \text{(A.64)}$$

$$W_T(q) = -\frac{1}{q^2}W_S(q) = \frac{g_A^2}{128\pi f_\pi^4 M_N}\left[g_A^2(3m_\pi^2 +q^2) - w^2\right]A(q)\,, \quad \text{(A.65)}$$

$$V_{LS}(q) = \frac{3g_A^4}{32\pi f_\pi^4 M_N}\,(2m_\pi^2+q^2)A(q)\,, \quad \text{(A.66)}$$

$$W_{LS}(q) = \frac{g_A^2(1-g_A^2)}{32\pi f_\pi^4 M_N}\,w^2 A(q)\,. \quad \text{(A.67)}$$

Spectral functions:

$$\mathrm{Im}V_C(i\mu) = \frac{3g_A^4}{512 f_\pi^4 M_N}\left[2m_\pi^5\delta(\mu^2-4m_\pi^2) - \frac{(2m_\pi^2-\mu^2)(m_\pi^2+\mu^2)}{\mu}\right], \quad \text{(A.68)}$$

$$\mathrm{Im}W_C(i\mu) = \frac{g_A^2}{256 f_\pi^4 M_N}\left\{6g_A^2 m_\pi^5\delta(\mu^2-4m_\pi^2) + \frac{(2m_\pi^2-\mu^2)\left[\mu^2-2m_\pi^2+g_A^2(3m_\pi^2-2\mu^2)\right]}{\mu}\right\}, \quad \text{(A.69)}$$

$$\mathrm{Im}V_S(i\mu) = \mu^2\,\mathrm{Im}V_T(i\mu) = \frac{3g_A^4\mu}{1024 f_\pi^4 M_N}(5m_\pi^2-2\mu^2)\,, \quad \text{(A.70)}$$

$$\mathrm{Im}W_S(i\mu) = \mu^2\,\mathrm{Im}W_T(i\mu) = \frac{g_A^2\mu}{512 f_\pi^4 M_N}(g_A^2(3m_\pi^2-\mu^2)+\mu^2-4m_\pi^2)\,, \quad \text{(A.71)}$$

$$\mathrm{Im}V_{LS}(i\mu) = \frac{3g_A^4}{128\mu f_\pi^4 M_N}\,(2m_\pi^2-\mu^2)\,, \quad \text{(A.72)}$$

$$\mathrm{Im}W_{LS}(i\mu) = \frac{g_A^2(1-g_A^2)}{128\mu f_\pi^4 M_N}\,(4m_\pi^2-\mu^2)\,. \quad \text{(A.73)}$$

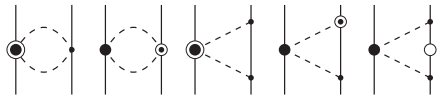

Figure A.3: Relativistic corrections of NNLO diagrams. Notation as in Fig. 2.1. Open circles are relativistic $1/M_N$ corrections.

Position-space potentials:

$$\begin{aligned}
\widetilde{V}_C(r) &= \frac{3g_A^4 m_\pi^6}{1024\pi^2 f_\pi^4 M_N}\frac{e^{-2x}}{x^6}(24+48x+46x^2 \\
&\quad +28x^3+10x^4+x^5)\,, \qquad \text{(A.74)}\\
\widetilde{W}_C(r) &= \frac{g_A^2 m_\pi^6}{512\pi^2 f_\pi^4 M_N}\frac{e^{-2x}}{x^6}(24(2g_A^2-1)(1+2x) \\
&\quad +(82g_A^2-40)x^2+(36g_A^2-16)x^3 \\
&\quad +(10g_A^2-4)x^4+3g_A^2x^5)\,, \qquad \text{(A.75)}\\
\widetilde{V}_S(r) &= -\frac{g_A^4 m_\pi^6}{512\pi^2 f_\pi^4 M_N}\frac{e^{-2x}}{x^6}(24+48x+43x^2 \\
&\quad +22x^3+6x^4)\,, \qquad \text{(A.76)}\\
\widetilde{V}_T(r) &= \frac{g_A^4 m_\pi^6}{1024\pi^2 f_\pi^4 M_N}\frac{e^{-2x}}{x^6}(48+96x+76x^2 \\
&\quad +31x^3+6x^4)\,, \qquad \text{(A.77)}\\
\widetilde{W}_S(r) &= -\frac{g_A^2 m_\pi^6}{1536\pi^2 f_\pi^4 M_N}\frac{e^{-2x}}{x^6}(24(g_A^2-1)(1+2x) \\
&\quad +2(21g_A^2-20)x^2+4(5g_A^2-4)x^3+4g_A^2x^4)\,, \qquad \text{(A.78)}\\
\widetilde{W}_T(r) &= \frac{g_A^2 m_\pi^6}{3072\pi^2 f_\pi^4 M_N}\frac{e^{-2x}}{x^6}(48(g_A^2-1)(1+2x) \\
&\quad +8(9g_A^2-8)x^2+2(13g_A^2-8)x^3+4g_A^2x^4)\,, \qquad \text{(A.79)}\\
\widetilde{V}_{LS}(r) &= -\frac{3g_A^4 m_\pi^6}{64\pi^2 f_\pi^4 M_N}\frac{e^{-2x}}{x^6}(1+x)(2+2x+x^2)\,, \qquad \text{(A.80)}\\
\widetilde{W}_{LS}(r) &= \frac{g_A^2(g_A^2-1)m_\pi^6}{32\pi^2 f_\pi^4 M_N}\frac{e^{-2x}}{x^6}(1+x)^2\,. \qquad \text{(A.81)}
\end{aligned}$$

A.5 Relativistic c_i/M_N corrections

At N^{3}LO, we add the $1/M_N$ correction of the NNLO 2PE proportional to c_i. This correction is proportional to c_i/M_N (Fig. A.3) and appears nominally at fifth order. As discussed,

the 2PE bubble diagram proportional to c_i^2 that appears at N^{3}LO is unrealistically attractive, while the c_i/M_N correction is large and repulsive. Therefore, it makes sense to group these diagrams together to arrive at a more realistic intermediate attraction at N^{3}LO. The contribution is given by [57]:

Momentum-space potentials:

$$\begin{aligned}
V_C(q) &= -\frac{g_A^2 L(q)}{32\pi^2 M_N f_\pi^4}\Big[(c_2-6c_3)q^4+4(6c_1+c_2-3c_3)q^2m_\pi^2 \\
&\quad +6(c_2-2c_3)m_\pi^4+24(2c_1+c_3)m_\pi^6 w^{-2}\Big]\,, \qquad \text{(A.82)}\\
W_C(q) &= -\frac{c_4 q^2 L(q)}{192\pi^2 M_N f_\pi^4}\Big[g_A^2(8m_\pi^2+5q^2)+w^2\Big]\,, \qquad \text{(A.83)}\\
W_T(q) &= -\frac{1}{q^2}W_S(q) = -\frac{c_4 L(q)}{192\pi^2 M_N f_\pi^4}\Big[g_A^2(16m_\pi^2 \\
&\quad +7q^2)-w^2\Big]\,, \qquad \text{(A.84)}\\
V_{LS}(q) &= \frac{c_2 g_A^2}{8\pi^2 M_N f_\pi^4}w^2 L(q)\,, \qquad \text{(A.85)}\\
W_{LS}(q) &= -\frac{c_4 L(q)}{48\pi^2 M_N f_\pi^4}\left[g_A^2(8m_\pi^2+5q^2)+w^2\right]\,. \qquad \text{(A.86)}
\end{aligned}$$

Spectral functions:

$$\begin{aligned}
\mathrm{Im}V_C(i\mu) &= \frac{g_A^2}{64\pi M_N f_\pi^4}\frac{\sqrt{\mu^2-4m_\pi^2}}{\mu}\Big[(c_2-6c_3)\mu^4-4(6c_1+c_2-3c_3)\mu^2m_\pi^2 \\
&\quad +6(c_2-2c_3)m_\pi^4-24(2c_1+c_3)\frac{m_\pi^6}{\mu^2-4m_\pi^2}\Big]\,, \qquad \text{(A.87)}\\
\mathrm{Im}W_C(i\mu) &= -\frac{c_4}{384\pi M_N f_\pi^4}\mu\sqrt{\mu^2-4m_\pi^2}\Big[g_A^2(8m_\pi^2-5\mu^2)-\mu^2+4m_\pi^2\Big]\,, \qquad \text{(A.88)}\\
\mathrm{Im}W_T(i\mu) &= \frac{1}{\mu^2}\mathrm{Im}W_S(i\mu) = \frac{c_4}{384\pi M_N f_\pi^4}\frac{\sqrt{\mu^2-4m_\pi^2}}{\mu}\Big[\mu^2-4m_\pi^2 \\
&\quad +g_A^2(16m_\pi^2-7\mu^2)\Big]\,, \qquad \text{(A.89)}\\
\mathrm{Im}V_{LS}(i\mu) &= \frac{c_2 g_A^2}{16\pi M_N f_\pi^4}\frac{(\mu^2-4m_\pi^2)^{3/2}}{\mu}\,, \qquad \text{(A.90)}\\
\mathrm{Im}W_{LS}(i\mu) &= \frac{c_4}{96\pi M_N f_\pi^4}\frac{\sqrt{\mu^2-4m_\pi^2}}{\mu}\left[g_A^2(8m_\pi^2-5\mu^2)+4m_\pi^2-\mu^2\right]\,. \qquad \text{(A.91)}
\end{aligned}$$

Position-space potentials:

$$\widetilde{V}_C(r) = \frac{3g_A^2 m_\pi^7}{32\pi^3 M_N f_\pi^4}\frac{1}{x^6}\Bigg[\Bigg(20(c_2-6c_3)-4(6c_1-c_2+9c_3)x^2 -2(2c_1+c_3)x^4\Bigg)xK_0(2x)+\Bigg(20(c_2-6c_3)-2(12c_1 -7c_2+48c_3)x^2-(16c_1-c_2+10c_3)x^4\Bigg)K_1(2x)\Bigg], \quad \text{(A.92)}$$

$$\widetilde{W}_C(r) = \frac{c_4 m_\pi^7}{32\pi^3 M_N f_\pi^4}\frac{1}{x^5}\Bigg[\Bigg(5+25g_A^2+4g_A^2x^2\Bigg)xK_1(2x) +2\Bigg(5+25g_A^2+(1+8g_A^2)x^2\Bigg)K_2(2x)\Bigg], \quad \text{(A.93)}$$

$$\widetilde{W}_S(r) = \frac{c_4 m_\pi^7}{48\pi^3 M_N f_\pi^4}\frac{1}{x^5}\Bigg[\Bigg(5-35g_A^2-4g_A^2x^2\Bigg)xK_1(2x) +2\Bigg(5(1-7g_A^2)+(1-10g_A^2)x^2\Bigg)K_2(2x)\Bigg], \quad \text{(A.94)}$$

$$\widetilde{W}_T(r) = \frac{c_4 m_\pi^7}{192\pi^3 M_N f_\pi^4}\frac{1}{x^5}\Bigg[2\Bigg(-8+59g_A^2+4g_A^2x^2\Bigg)xK_1(2x) -\Bigg(35(1-7g_A^2)+4(1-13g_A^2)x^2\Bigg)K_2(2x)\Bigg], \quad \text{(A.95)}$$

$$\widetilde{V}_{LS}(r) = \frac{3c_2 g_A^2 m_\pi^7}{8\pi^3 M_N f_\pi^4}\frac{1}{x^5}\Bigg[K_2(2x)+2xK_3(2x)\Bigg], \quad \text{(A.96)}$$

$$\tilde{W}_{LS}(r) = -\frac{c_4 m_\pi^7}{16\pi^3 M_N f_\pi^4}\frac{1}{x^5}\Bigg[(1+6g_A^2)2xK_1(2x) +(5+25g_A^2+4g_A^2x^2)K_2(2x)\Bigg]. \quad \text{(A.97)}$$

APPENDIX B

The LECs of the contact terms

In this Appendix, we show in Table B.1 the LECs of the contact terms defined in Sec. 2.4 for our N^{3}LO potentials. The shown LECs are the coefficients of the various contact operators displayed in Sec. 2.4.

For the fitting of the phase shifts of the different states, it is more convenient to fit to states with well-defined total spin S and total isospin T, the LO coefficients of which we denote by C_{ST}. From these C_{ST}, one obtains the coefficients for the operators used in Eq. (2.19) via:

$$\begin{pmatrix} C_c \\ C_\tau \\ C_\sigma \\ C_{\sigma\tau} \end{pmatrix} = \frac{1}{16} \begin{pmatrix} 1 & 3 & 3 & 9 \\ -1 & 1 & -3 & 1 \\ -1 & -3 & 1 & 3 \\ 1 & -1 & -1 & 1 \end{pmatrix} \begin{pmatrix} C_{00} \\ C_{01} \\ C_{10} \\ C_{11} \end{pmatrix} \tag{B.1}$$

Similar relations apply to the central force LECs of higher order, like the C_1 to C_4 of Eq. (2.23) and the D_1 to D_4 of Eq. (2.30); as well to the coefficients of the four $\vec{L}^2$ terms, D_{11} to D_{14} [Eq. (2.30)].

Vice versa, the spin-isopin coefficients can be obtained from the operator LECs via:

$$\begin{pmatrix} C_{00} \\ C_{01} \\ C_{10} \\ C_{11} \end{pmatrix} = \begin{pmatrix} 1 & -3 & -3 & 9 \\ 1 & 1 & -3 & -3 \\ 1 & -3 & 1 & -3 \\ 1 & 1 & 1 & 1 \end{pmatrix} \begin{pmatrix} C_c \\ C_\tau \\ C_\sigma \\ C_{\sigma\tau} \end{pmatrix} \tag{B.2}$$

Tensor, spin-orbit, and quadratic spin-orbit terms exist only in $S = 1$ states, such that one needs to distinguish only between a $T = 0$ and $T = 1$ channel. For the case of the NLO

Table B.1: Values for the contact LECs of the N^{3}LO potentials with cutoff combination $(R_\pi, R_{\rm ct}) = (1.2, 0.75)$ fm, $(1.1, 0.72)$ fm, and $(1.0, 0.70)$ fm. In the column headings, we use the R_π value to identify the different cases. The notation $(\pm n)$ stands for $\times 10^{\pm n}$.

LECs	$R_\pi = 1.2$ fm	$R_\pi = 1.1$ fm	$R_\pi = 1.0$ fm
C_c^{np} (fm^2)	0.28717299 (+1)	0.39490035 (+1)	0.68499330 (+1)
C_τ^{np} (fm^2)	0.26560171	0.36862166	0.84342750
C_σ^{np} (fm^2)	0.46462631 (-1)	0.14012451	0.46431300
$C_{\sigma\tau}^{np}$ (fm^2)	0.10005058 (+1)	0.87076834	0.90360050
C_c^{pp} (fm^2)	0.28878741 (+1)	0.39655771 (+1)	0.68647468 (+1)
C_τ^{pp} (fm^2)	0.27098312	0.37414619	0.84836544
C_σ^{pp} (fm^2)	0.30318375 (-1)	0.12355094	0.44949919
$C_{\sigma\tau}^{pp}$ (fm^2)	0.99512437	0.86524381	0.89866256
C_c^{nn} (fm^2)	0.28830563 (+1)	0.39601604 (+1)	0.68602361 (+1)
C_τ^{nn} (fm^2)	0.26937719	0.37234063	0.84686187
C_σ^{nn} (fm^2)	0.35136188 (-1)	0.12896763	0.45400987
$C_{\sigma\tau}^{nn}$ (fm^2)	0.99673031	0.86704937	0.90016612
C_1 (fm^4)	0.20339187 (-1)	-0.69958000 (-1)	-0.19849806
C_2 (fm^4)	-0.26911188 (-1)	-0.73932500 (-2)	0.27128125 (-2)
C_3 (fm^4)	-0.78260937 (-1)	-0.57466500 (-1)	-0.26448938 (-1)
C_4 (fm^4)	-0.35220625 (-2)	-0.13702250 (-1)	-0.89698125 (-2)
C_5 (fm^4)	-0.10596750 (-1)	-0.80355000 (-2)	-0.54697500 (-2)
C_6 (fm^4)	0.31287500 (-2)	0.39985000 (-2)	0.48457500 (-2)
C_7 (fm^4)	-0.84559075	-0.83002375	-0.82673000
C_8 (fm^4)	-0.11612925	-0.10974825	-0.10887000
D_1 (fm^6)	0.27843312 (-1)	0.31251437 (-1)	0.35406750 (-1)
D_2 (fm^6)	-0.11181250 (-3)	0.30660625 (-2)	0.64797500 (-2)
D_3 (fm^6)	0.17309375 (-2)	0.39478125 (-2)	0.28025000 (-2)
D_4 (fm^6)	-0.25564375 (-2)	-0.11373125 (-2)	-0.84200000 (-3)
D_5 (fm^6)	-0.22787500 (-2)	-0.17605000 (-2)	0.13175000 (-3)
D_6 (fm^6)	-0.76425000 (-3)	-0.58650000 (-3)	0.44250000 (-4)
D_7 (fm^6)	0.40027500 (-2)	0.11374250 (-1)	0.70485000 (-2)
D_8 (fm^6)	-0.26426750 (-1)	-0.22689250 (-1)	-0.29755500 (-1)
D_9 (fm^6)	-0.42584000 (-1)	-0.50699750 (-1)	-0.57539750 (-1)
D_{10} (fm^6)	-0.14453000 (-1)	-0.16889250 (-1)	-0.19163250 (-1)
D_{11} (fm^6)	-0.18565375 (-1)	-0.27816625 (-1)	-0.63730625 (-2)
D_{12} (fm^6)	0.16119625 (-1)	0.11181125 (-1)	0.20284813 (-1)
D_{13} (fm^6)	0.54308750 (-2)	0.25901250 (-2)	0.77255625 (-2)
D_{14} (fm^6)	0.92428750 (-2)	0.76783750 (-2)	0.10042688 (-1)

tensor force, the relations are:

$$C_5 = \frac{1}{4}\left(C_{T=0}^{(S_{12})} + 3C_{T=1}^{(S_{12})}\right), \tag{B.3}$$

$$C_6 = \frac{1}{4}\left(-C_{T=0}^{(S_{12})} + C_{T=1}^{(S_{12})}\right), \tag{B.4}$$

and vice versa

$$C_{T=0}^{(S_{12})} = C_5 - 3C_6\,, \tag{B.5}$$

$$C_{T=1}^{(S_{12})} = C_5 + C_6\,, \tag{B.6}$$

and similarly for the other cases that appear only at $S = 1$.

APPENDIX C

Phase-shift tables

In this Appendix, we show the phase shifts as predicted by the *pp*, *np*, and *nn* N^{3}LO potentials with cutoff combination $(R_\pi, R_{\rm ct}) = (1.0, 0.70)$ fm in Tables C.1-C.4. Note that our *pp* phase shifts are the phase shifts of the nuclear plus relativistic Coulomb interaction with respect to Coulomb wave functions. For *nn* and *np* scattering, our phase shifts are the ones from the nuclear interaction with respect to Riccati-Bessel functions. For more of the technical details of our phase shift calculations, see Appendix A3 of Ref. [36].

Table C.1: *pp* phase shifts (in degrees) up to F waves at N^{3}LO with cutoff combination $(R_\pi, R_{\rm ct}) = (1.0, 0.70)$ fm.

$T_{\rm lab}$ (MeV)	$^1S_0$	$^3P_0$	$^3P_1$	$^1D_2$	$^3P_2$	$^3F_2$	ϵ_2	$^3F_3$	$^1G_4$	$^3F_4$
1	32.82	0.14	-0.08	0.00	0.01	0.00	0.00	0.00	0.00	0.00
5	55.02	1.60	-0.89	0.04	0.22	0.00	-0.05	0.00	0.00	0.00
10	55.49	3.78	-2.03	0.17	0.67	0.01	-0.20	-0.03	0.00	0.00
25	49.15	8.68	-4.86	0.70	2.52	0.11	-0.82	-0.23	0.04	0.02
50	39.68	11.54	-8.25	1.70	5.84	0.35	-1.75	-0.69	0.16	0.12
100	26.12	9.19	-13.29	3.69	10.98	0.83	-2.82	-1.50	0.44	0.51
150	16.15	4.07	-17.51	5.46	13.98	1.13	-3.19	-2.10	0.73	1.05
200	8.12	-1.40	-21.24	6.88	15.49	1.16	-3.19	-2.55	1.03	1.66

Table C.2: nn phase shifts (in degrees) up to F waves at N^{3}LO with cutoff combination $(R_\pi, R_{\rm ct}) = (1.0, 0.70)$ fm.

$T_{\rm lab}$ (MeV)	$^1S_0$	$^3P_0$	$^3P_1$	$^1D_2$	$^3P_2$	$^3F_2$	ϵ_2	$^3F_3$	$^1G_4$	$^3F_4$
1	57.68	0.21	-0.12	0.00	0.02	0.00	0.00	0.00	0.00	0.00
5	61.18	1.87	-1.03	0.05	0.27	0.00	-0.06	-0.01	0.00	0.00
10	58.08	4.15	-2.22	0.18	0.77	0.01	-0.22	-0.04	0.00	0.00
25	49.58	9.02	-5.10	0.73	2.71	0.11	-0.85	-0.24	0.04	0.02
50	39.44	11.66	-8.50	1.75	6.12	0.36	-1.78	-0.70	0.16	0.13
100	25.60	9.04	-13.57	3.77	11.26	0.84	-2.83	-1.52	0.44	0.52
150	15.56	3.79	-17.81	5.56	14.20	1.14	-3.18	-2.12	0.74	1.07
200	7.49	-1.74	-21.56	6.99	15.64	1.15	-3.16	-2.57	1.04	1.69

Table C.3: $T = 1$ np phase shifts (in degrees) up to F waves at N^{3}LO with cutoff combination $(R_\pi, R_{\rm ct}) = (1.0, 0.70)$ fm.

$T_{\rm lab}$ (MeV)	$^1S_0$	$^3P_0$	$^3P_1$	$^1D_2$	$^3P_2$	$^3F_2$	ϵ_2	$^3F_3$	$^1G_4$	$^3F_4$
1	62.07	0.18	-0.11	0.00	0.02	0.00	0.00	0.00	0.00	0.00
5	63.62	1.63	-0.92	0.04	0.26	0.00	-0.05	0.00	0.00	0.00
10	59.95	3.68	-2.03	0.16	0.73	0.01	-0.18	-0.03	0.00	0.00
25	50.87	8.22	-4.79	0.68	2.60	0.09	-0.76	-0.20	0.03	0.02
50	40.41	10.77	-8.17	1.71	5.91	0.31	-1.66	-0.61	0.14	0.11
100	26.34	8.25	-13.25	3.78	10.98	0.77	-2.73	-1.39	0.41	0.48
150	16.20	3.11	-17.52	5.62	13.92	1.05	-3.12	-1.96	0.71	1.01
200	8.07	-2.36	-21.29	7.08	15.39	1.06	-3.14	-2.40	1.02	1.62

Table C.4: $T = 0$ np phase shifts (in degrees) up to F waves at N^{3}LO with cutoff combination $(R_\pi, R_{\rm ct}) = (1.0, 0.70)$ fm.

$T_{\rm lab}$ (MeV)	$^1P_1$	$^3S_1$	$^3D_1$	ϵ_1	$^3D_2$	$^1F_3$	$^3D_3$	$^3G_3$	ϵ_3	$^3G_4$
1	-0.19	147.73	-0.01	0.10	0.01	0.00	0.00	0.00	0.00	0.00
5	-1.49	118.14	-0.18	0.59	0.22	-0.01	0.00	0.00	0.01	0.00
10	-3.03	102.55	-0.66	0.97	0.85	-0.07	0.01	0.00	0.08	0.01
25	-6.22	80.54	-2.73	1.27	3.74	-0.42	0.04	-0.05	0.56	0.17
50	-9.31	62.65	-6.32	1.01	9.02	-1.13	0.31	-0.26	1.63	0.73
100	-13.62	43.16	-12.26	0.09	17.23	-2.18	1.42	-0.98	3.58	2.23
150	-17.59	30.85	-17.00	-0.83	21.87	-2.79	2.70	-1.88	4.98	3.78
200	-21.50	21.71	-21.02	-1.72	24.00	-3.16	3.67	-2.86	5.92	5.23